The effect of a forward-facing step on Tollmien–Schlichting waves

Barahona, M.; Rius Vidales, A.F.; Tocci, Francesco ; Hein, Stefan; Kotsonis, M.

DOI
10.1017/jfm.2025.10768

Publication date
2025

Document Version
Final published version

Published in
Journal of Fluid Mechanics

J. Fluid Mech. (2025), *vol.* 1023, A38, doi:10.1017/jfm.2025.10768

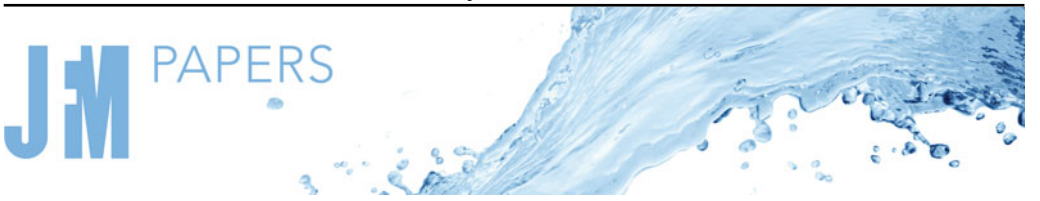

The effect of a forward-facing step on Tollmien–Schlichting waves

Marina Barahona[1], **Alberto Felipe Rius-Vidales**[2], **Francesco Tocci**[3], **Stefan Hein**[3] **and Marios Kotsonis**[1]

[1]Department of Flow Physics and Technology, Faculty of Aerospace Engineering, Delft University of Technology, Kluyverweg 1, 2629 HS Delft, The Netherlands

[2]Maritime and Transport Technology, Faculty of Mechanical Engineering, Delft University of Technology, 2628 CD Delft, The Netherlands

[3]Department of High Speed Configurations, Institute of Aerodynamics and Flow Technology, German Aerospace Center DLR, Bunsenstr. 10, 37073 Göttingen, Germany

Corresponding author: Marina Barahona, M.BarahonaLopez@tudelft.nl

(Received 27 February 2025; revised 10 July 2025; accepted 19 September 2025)

The interaction between a forward-facing step (FFS) and single-frequency Tollmien–Schlichting (TS) waves is investigated with experiments and two-dimensional (2-D) direct numerical simulations (DNS). Dedicated hot-wire anemometry and particle image velocimetry measurements in the vicinity of the FFS provide characterisation of the perturbation field, as well as validation of the DNS results. Comparison between experiments, 2-D DNS, and linear parabolised stability equations confirm the 2-D nature of the flow and the linearity of the instability mechanisms around the FFS. Upstream of the step, TS waves are gradually amplified by the increasing adverse pressure gradient. In the step vicinity, both mean flow and perturbation field exhibit abrupt distortion, with decoupling of the base flow-oriented growth rate components indicating significant non-modal evolution. Downstream of the step, the mean flow recovers to baseline conditions, but the perturbation field remains highly distorted. Linear stability theory results suggest the presence of superimposed modes on the original TS mode in this region. Despite their decay in the streamwise direction, their presence imprints modifications in the TS wave growth and shape, manifested as the tilting of the perturbation structure in and against the mean flow shear direction. This initiates a reversed Orr mechanism, characterised by a region of stabilisation followed by destabilisation further downstream. Eventually, the TS waves realign to their asymptotic (modal) behaviour. Overall, the FFS destabilises the TS wave far downstream. However, the streamwise extent and magnitude of the stabilisation downstream of the FFS remain significant.

Key words: boundary layer stability, absolute/convective instability, transition to turbulence

1. Introduction

Laminar flow control (LFC) emerges as a promising technology to reduce skin-friction drag in modern high subsonic aircraft. Delaying laminar-to-turbulent transition to 40 % of the wing chord can reduce total drag by up to 11 % (Schrauf 2005). However, several studies (e.g. Schrauf 2005; Hansen 2010) have demonstrated that LFC efficiency is highly dependent on the wing surface finish. Of particular importance are spanwise-distributed roughness like steps and gaps, which drastically modify the boundary-layer stability, causing premature laminar-to-turbulent transition (Crouch, Kosorygin & Ng 2006).

The primary aerodynamic surfaces of passenger aircraft, namely the wing and tail, typically feature moderate sweep angles. Consequently, the study of swept-wing aerodynamics is crucial for enhancing overall aircraft efficiency. Two main instabilities lead to laminar-to-turbulent transition on swept wings: Tollmien–Schlichting (TS) waves and crossflow instability (CFI). For low to moderate sweep angles ($0°-25°$, see Joslin 1998), TS waves govern the laminar flow breakdown, while CFI governs transition at higher sweep angles (Joslin 1998). Thus, laminar-to-turbulent transition over the wings of commercial transport aircraft – featuring sweep angles below 35° – results from the combination of both TS and CFI growth (Mack 1984). This study will focus on the effect of a two-dimensional (2-D) forward-facing step (FFS) on the laminar-to-turbulent transition dominated by TS waves.

1.1. *Effect of a FFS on transition location*

Steps and gaps often form at the intersection of wing panels, posing a significant challenge to the practical application of LFC techniques, especially near the leading edge (LE) at the wing-box junction (Schrauf 2005). Driven by the engineering needs of aircraft manufacturers, initial research on FFS-induced transition aimed to determine a critical Reynolds height parameter ($Re_{h,crit} = h_{crit}U/\nu$) to identify the maximum permissible step height between panel discontinuities that would avoid laminar-to-turbulent transition at the step location. In what follows, the Reynolds height (Re_h) is defined using the free-stream velocity (U) and kinematic viscosity (ν) at the step location (x_s), with h denoting the step height. Early experiments by Nenni & Gluyas (1966) established a critical FFS height parameter of $Re_{h,crit} = 1800$. Later, a series of experiments performed by the Northrop Grumman Corporation (Drake *et al.* 2008, 2010) on an unswept wing with gap and step geometries revealed that, in the case of FFS, larger step heights ($Re_{h,crit} \geqslant 1800$) did not significantly advance transition. A similar conclusion was drawn from the results of the European collaborative F100 and ATTAS flight tests, which led to an increase in the permissible critical Reynolds number with FFS to $Re_{h,crit} = 3600$ (Schrauf 2018).

The variation in $Re_{h,crit}$ between the aforementioned studies indicates the lack of universality of this criterion in predicting a critical FFS height. In view of this, several researchers adopted a more comprehensive approach to estimate the change of transition location with different FFS heights. This approach is based on the e^N method, whereby knowing the increase in N factor in the presence of a step ($\Delta N = N_{step} - N_0$), the movement of the transition front can be estimated with respect to the no-step (baseline) case. Following this idea, Perraud & Seraudie (2000), Wang & Gaster (2005) and Crouch *et al.* (2006) proposed different semi-empirical models to isolate the effect of the relative step height (h/δ^*) on the transition location using a single parameter, namely ΔN. In literature, the relative step height or h/δ^* is defined as the ratio between the step height (h) and the displacement thickness (δ^*) measured at the step location (x_s) in no-step (baseline) conditions. The experiments of Wang & Gaster (2005) on a flat plate in

subsonic conditions presented a good correlation between the relative step height (h/δ^*) and ΔN for FFS. In addition, Crouch *et al.* (2006) proposed a linear correlation of $\Delta N = 1.6h/\delta^*$, accounting for both adverse and favourable pressure gradients effects. In a recent experimental work, Methel *et al.* (2022) compared the correlation of Crouch *et al.* (2006) with ΔN measurements downstream of various surface defects (including FFS) subject to different levels of distributed wall suction. In agreement with Crouch *et al.* (2006), their ΔN results confirmed a linear increase with h/δ^* (see figure 13 in Methel *et al.* 2022).

Following the need to understand the effect of Mach number, pressure gradient and wall temperature on TS–FFS laminar-to-turbulent transition, Costantini, Risius & Klein (2022) conducted an extensive experimental study featuring a wide range of different step heights and free-stream conditions on an unswept flat-plate model. When comparing the best $\Delta N = f(h/\delta^*)$ fit to their experimental data with the models proposed by Wang & Gaster (2005) and Crouch *et al.* (2006), Costantini *et al.* (2022) observed discrepancies. In Costantini (2016), the author attributes the disagreement to possible differences in step geometries, step locations, transition detection techniques or the nature of the baseline laminar-to-turbulent transition.

The observed disagreement between the different ΔN models puts into question whether the transition location resulting from the interaction between TS waves and FFS can be fully encapsulated within two parameters, namely ΔN and h/δ^*. The persistent inability of single or double parameter correlations to universally capture transition location under these conditions points to a more complex problem of flow interaction. Further elucidation of the flow mechanisms at play in the step vicinity can help determine the governing parameters of the TS–FFS interaction and whether they are bounded by functional relations. While establishing specific functional relationships between step parameters and transition location (i.e. ΔN models) is not in the scope of the present study, the analysis and clarification of the perturbation behaviour around the step presented here represents an initial step towards that goal.

1.2. *Effect of a FFS on the development and growth of TS waves*

The work of Wörner *et al.* (2003) constitutes one of the first detailed numerical studies reporting the growth and evolution of a TS wave in the neighbourhood of a FFS. The authors used direct numerical simulations (DNS) to investigate the interaction of a TS wave with reduced frequency $F = (2\pi f \nu/U^2) \cdot 10^6 = 49.34$ in the presence of a small FFS, namely $h/\delta^* = 0.235$. In Wörner *et al.* (2003), assuming viscosity in air at sea level conditions ($\nu = 1.46 \times 10^{-5}$ m^2 s^{-1}), the TS wave dimensional frequency is $f = 2$ Hz, with $U = 1.93$ m s^{-1}. Interestingly, the results of Wörner *et al.* (2003) show TS wave stabilisation downstream of the step. The authors ascribed this behaviour to the origin of a thinner and more stable boundary layer downstream of the step edge and to the absence of free-stream disturbances.

Recently, Dong & Zhang (2018) revisited the TS–FFS case of Wörner *et al.* (2003) using a local scattering approach, which relies on asymptotic triple-deck theory to simulate the effect of a disturbance encountering a local scatterer, i.e. surface discontinuity. Dong & Zhang (2018) found that, in line with previous numerical (Rizzetta & Visbal 2014) and experimental (Wang & Gaster 2005; Costantini *et al.* 2022) works, both FFS and backward-facing steps destabilise the incoming TS waves. Similar to the results of Wörner *et al.* (2003), Dong & Zhang (2018) also report a local attenuation of TS waves below baseline values downstream of the step. However, contrary to Wörner *et al.* (2003), the TS wave was found to amplify again further downstream, eventually exceeding baseline amplitude levels.

Similar to Wörner *et al.* (2003), recent works (Xu, Lombard & Sherwin 2017; Teng 2023) have also reported stabilisation of TS waves in the presence of small steps, often referred to as subcritical. Introducing Gaussian white noise, Xu *et al.* (2017) resolved both K- and H-type transition scenarios in the presence of a so-called smooth step. The smooth step described in Xu *et al.* (2017) features a geometry similar to a smooth ramp or an elongated step, with a width comparable to one TS wavelength. The authors report attenuation and transition delay with smooth step heights of $h/\delta^* = 0.164$ and $h/\delta^* = 0.384$, subject to a TS wave with a reduced frequency of $F = 150$. Compared with the destabilisation reported with sharp FFS (Edelmann 2014), the stabilisation observed with smooth steps was attributed to the absence of recirculating flow (i.e. laminar separation bubbles) in the vicinity of the steps (Xu *et al.* 2017). Similarly, other researchers have also reported significant differences in the stability of TS waves between sharp steps and steps featuring a rounded edge, with the latter showing a reduced impact on laminar-to-turbulent transition (Holmes *et al.* 1985; Franco, Hein & Valero 2020).

Recently, Teng (2023) reported significant transition delay with a sharp FFS. The author used DNS to simulate the development of K-type transition under two different FFS heights (large, $h/\delta^* = 1$, and medium, $h/\delta^* = 0.5$), subject to a single-frequency TS forcing at $F = 100$. Similar to previous numerical results (Edelmann 2014; Dong & Zhang 2018), Teng (2023) also reports local attenuation of the TS wave shortly downstream of the step. However, different from the step cases studied in Dong & Zhang (2018), Teng (2023) finds a step case for which transition is delayed. In particular, the results of Teng (2023) show that, after the local attenuation, TS waves resume growth for the highest step ($h/\delta^* = 1$), while for the smallest step ($h/\delta^* = 0.5$), TS waves continue decaying below baseline values.

Edelmann (2014) conducted an extensive DNS study investigating the interaction between TS waves and FFS in both subsonic and supersonic flow regimes. The author compared the growth predicted by linear stability theory (LST) with results from DNS in the presence of a FFS. The goal was to evaluate the accuracy of using ΔN models to predict transition location based on LST. In the subsonic regime, Edelmann (2014) observed significant disagreement between LST and DNS shortly downstream of the step, in the region where TS waves experience local attenuation. Inspection of the fundamental TS mode shape at this location revealed a strong deformation, which deviates significantly from the expected canonical modal TS mode shape (Edelmann 2014). Interestingly, the author points to the existence of strong non-modal growth in this region to explain the observed TS mode shape distortion in the DNS.

1.3. *Parallelisms between TS waves and stationary crossflow instabilities interacting with FFS*

Recent DNS and experiments in swept-wing boundary layers, where transition is governed by stationary crossflow instabilities (S-CFI), have also identified transition delay in the presence of a FFS, opening the door to a new passive flow control strategy for swept-wing laminar-to-turbulent transition. Rius-Vidales & Kotsonis (2021) performed experiments on a 45° swept wing and found that a relatively small FFS ($h/\delta^* = 0.83$) leads to a strong stabilisation effect on the primary S-CFI mode, resulting in an overall transition delay. Numerically, the DNS results from Casacuberta *et al.* (2022) confirmed a strong stabilisation of the primary CFI mode downstream of a FFS. Prior to these studies, the available literature pointed to an overall destabilising effect of FFS for S-CFI-dominated transition (Tufts *et al.* 2017; Eppink 2020; Rius-Vidales & Kotsonis

2020), alike observations with TS waves (Crouch *et al.* 2006; Drake *et al.* 2008; Perraud, Arnal & Kuehn 2014; Drake *et al.* 2010).

Similar to the findings reported for the TS–FFS interaction, a local region of CFI attenuation has also been observed shortly downstream of a FFS both in experiments (Rius-Vidales & Kotsonis 2021) and DNS (Casacuberta *et al.* 2022). The DNS results and analysis presented in Casacuberta *et al.* (2022) confirm that the observed stabilisation is primarily driven by linear mechanisms, inasmuch as it is completely described by the production term in the Reynolds–Orr equation. Additionally, shortly downstream of the step, results in Casacuberta *et al.* (2022) show that the primary crossflow wavefront appears strongly deformed and misaligned with the base flow streamlines. The authors relate the observed misalignment to regions where the perturbation might be subject to non-modal growth mechanisms, in line with the conclusions derived in Edelmann (2014) for TS waves.

1.4. *Scope and outline of the present work*

Overall, the mechanisms driving the development and stability of TS waves in the presence of a FFS remain unclear. Recent DNS findings (Teng 2023) showing stabilisation of TS waves and transition delay further emphasise the complexity of the TS–FFS interaction. This study aims to closely examine the perturbation dynamics at the step and identify the key mechanisms influencing the growth and evolution of TS waves.

This work constitutes an experimental and numerical investigation jointly conducted by the Delft University of Technology (TU Delft) and the German Aerospace Center (DLR) on TS waves interaction with a FFS ($h/\delta_0^* = 0.76$). Experiments are conducted at the TU Delft low-turbulence anechoic wind tunnel (A-tunnel) on an unswept flat-plate model, where single-frequency TS modes are excited using acoustic forcing. The temporal response of the flow in the vicinity of the step is captured using hot-wire anemometry (HWA), and their spatial topology is retrieved with particle image velocimetry (PIV). Additionally, 2-D DNS conducted at DLR provide detailed flow information at the step vicinity. In this work, experimental and DNS results are complementary, with the experimental data providing empirical observations and the DNS offering detailed analysis of the flow dynamics near the step. Together, they contribute to a more comprehensive understanding of the flow behaviour.

This study is organised as follows. Section 2 describes the flow configuration, experimental set-up, wind tunnel model, perturbation forcing and measurement techniques. Additionally, the numerical set-up of DNS and boundary-layer stability tools is introduced. Section 3 presents experimental and numerical results on mean flow modifications induced by the step. Section 4 examines perturbation field distortions near the FFS, comparing DNS and experimental data. Section 5 investigates the stability characteristics and underlying mechanisms governing the perturbation dynamics observed in § 4. Finally, § 6 summarises the main findings of this study.

2. Methodology

2.1. *Selection of FFS heights and flow conditions*

The goal of this study is to describe the behaviour of TS waves as they interact with the step and understand pertinent modifications on their growth and spatio-temporal evolution. To do so, the FFS geometry and size are chosen as such to significantly destabilise the incoming perturbations but not trip the flow to turbulence immediately downstream.

The choice of geometrical step parameters is made based on the FFS configurations studied in previous works (e.g. Wang & Gaster 2005; and Edelmann 2014). Figure 1(*a*)

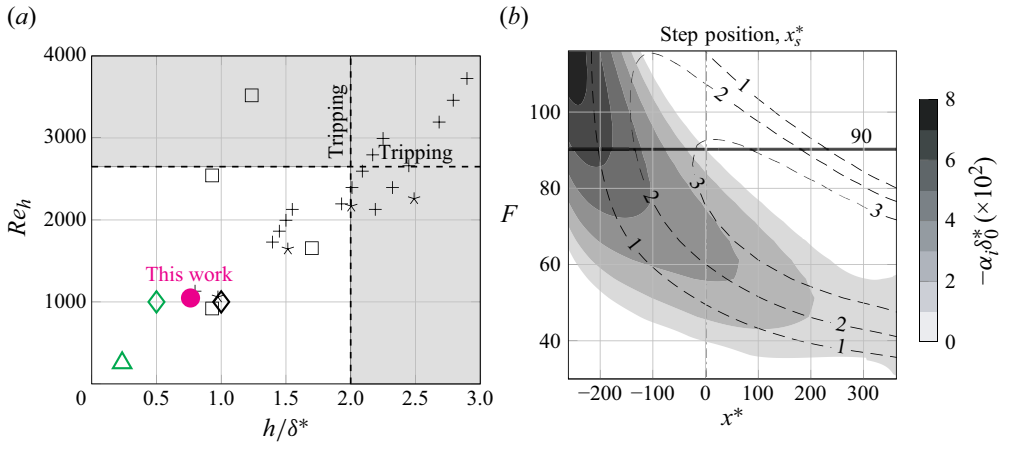

Figure 1. (*a*) The FFS configurations investigated in works studying the TS–FFS interaction. Greyed regions delimit the boundaries of Re_h and h/δ^* for which BL tripping at the step is reported from past experiments. Experimental works: Wang & Gaster (2005) (+), Perraud & Seraudie (2000) (∗) and this work (•). Numerical works: Edelmann (2014) (□), Teng (2023) (⋄) and Wörner *et al.* (2003) (△). Green symbols (e.g. ⋄) represent step configurations for which transition delay or stabilisation have been identified under specific TS wave conditions. (*b*) Stability diagram in baseline conditions from LST, where $x^* = (x - x_s)/\delta_0^*$. Contours indicate the growth rate (α_i) while dashed lines indicate the N factor. The horizontal grey line at $F = 90$ indicates the studied reduced frequency.

Case ID	$\overline{h}$ (μm)	$\overline{h}/\delta_0^*$	Re_h	U_0	c	$Re = U_0 c/\nu_0$	f	F	A	A/U_0
Baseline	−8	−0.009	−11	22.5 m s^{-1}	0.95 m	1.32×10^6	450 Hz	90	0.04 m s^{-1}	0.17 %
FFS	732	0.787	1017							

Table 1. Reference flow conditions, TS forcing parameters and FFS geometrical parameters. The amplitude and frequency of the forced TS wave are measured at $x^* = -43$ in baseline conditions. The reduced frequency is expressed as $F = (2\pi f \nu_0/U_0^2) \times 10^6$. The step is located at $x_s = 0.38$ m ($Re_s = U_0 x_s/\nu_0 = 5.3 \times 10^5$). The spanwise-averaged step height is denoted as $\overline{h}$, while the uniformity of the step height across the span is quantified by its standard deviation, measured as $\sigma_{\overline{h}} = 7$ μm. The reference displacement thickness is measured at the step location in baseline conditions, namely $\delta_0^* = 0.93$ mm.

shows the relative step height (h/δ^*) and Reynolds number ($Re_h = Uh/\nu$) from various experimental and numerical investigations covering the TS–FFS interaction and conducted at flow conditions similar to this work, i.e. at low Mach number (M <0.3) and nearly zero external pressure gradient. Note that δ^* is used to define the relative step height only when referring to other studies. When referring to the FFS studied in this work, the step height is explicitly normalised using $\delta_0^* = 0.93$ mm. The FFS configuration investigated herein is indicated in figure 1(*a*) and presented in table 1. In line with previous works, the displacement thickness at the step location under baseline conditions (δ_0^*) is used as the reference length scale to define the non-dimensional step height (h/δ_0^*). In this case, $\delta_0^* = 0.93$ mm, resulting in a relative step height of $h/\delta_0^* = 0.787$ (table 1). This constitutes a FFS that is expected to not trip the boundary-layer transition (note grey region in figure 1*a*) but neither delay it (note green symbols in figure 1*a*). Notably, the chosen FFS configuration is close to the smallest step investigated in Wang & Gaster (2005) (see + symbol in figure 1*a*), for which the authors reported a small transition advancement of $\Delta Re_{x_{tr}} \approx 3.3$ %.

In order to deterministically investigate the pertinent interactions at the step and ensure consistency between experimental and numerical approaches, a single frequency (i.e. monochromatic) TS mode is desired. This is achieved via external forcing, described in more detail in § 2.2.2.

The TS wave frequency is chosen based on the stability characteristics of the baseline case. For this, the base flow is obtained by solving the steady and incompressible boundary-layer equations, using the external velocity distribution ($U_e(x)$) retrieved from experiments as input. Thereafter, the stability of the base flow is computed by solving the Orr–Sommerfeld (OS) equation. Figure 1(*b*) shows the stability diagram in baseline flow conditions, indicated in table 1. The TS frequency studied in this work (table 1) constitutes a TS mode that achieves maximum amplitude ($N = 3$, dashed lines in figure 1*b*) at the step location. Under baseline conditions, this mode decays downstream of the step.

The influence of the TS mode frequency on the TS–FFS interaction was investigated by Rouviere (2023) using harmonic linearised Navier–Stokes equations. Their results (Rouviere 2023, figure 5.14) show that, under equivalent step height conditions, different TS modes – provided they are unstable at the step location under baseline conditions – exhibit similar growth behaviour downstream of the FFS. Based on these observations, and given that the main focus of this study is to identify the dominant flow mechanisms driving the TS–FFS interaction under linear conditions, the present analysis is restricted to a single representative mode (i.e. $F = 90$), which features the highest integral amplification at the step location based on the conditions of this study. Nevertheless, it is important to emphasise that, when aiming to capture the global effect of a FFS under natural transition, it is essential to consider a broader range of TS frequencies to effectively build the N-factor envelope.

2.2. *Experimental set-up and flow measurement techniques*

The experiments are conducted in the A-tunnel, an open-jet, closed-circuit, subsonic, vertical wind tunnel. The facility has undergone recent renovations to improve its acoustic and flow quality. This allowed for a suitable environment to force and study TS waves, given their high sensitivity to acoustic emissions and free-stream turbulence intensity. The modifications and results of the tunnel's aeroacoustic characterisation are described in detail by Merino-Martínez *et al.* (2020).

The free-stream velocity is fixed at $U_\infty = 20.5\ \mathrm{m\ s^{-1}}$ to obtain an external velocity over the measurement side of $U_0 = 22.5\ \mathrm{m\ s^{-1}}$. This enabled the chord-based Reynolds number to be kept at $Re = U_0 c/\nu_0 = 1.32 \times 10^6$ (variations due to room temperature changes remain within $\pm 1\ \%$ of Re) throughout the experiment to achieve similarity between the DNS and experimental conditions; see table 1. Under these free-stream conditions, the measured turbulence intensity was $T_u = \sqrt{u_{rms}^2 + v_{rms}^2}/(\sqrt{2}U_\infty) \leqslant 0.1\ \%$ (band-pass filtered between $2 \leqslant f_{bp} \leqslant 2 \times 10^3$ Hz).

The model geometry consists of an unswept flat plate featuring 0.95 m chord and 20 mm thickness, and spanning the rectangular test section with a cross-sectional area of $500 \times 500\ \mathrm{mm^2}$ (see figure 2). The flat plate is enclosed by four walls to minimise environmental disturbances and ensure the two-dimensionality of the flow in the measurement region. Additionally, to achieve nearly zero pressure gradient (ZPG) conditions over the region of interest, the top wall is slightly diverged from the bottom wall to account for boundary-layer growth at the wind tunnel walls. The maximum acceleration parameter $K = (\nu/U_e^2)(\mathrm{d}U_e/\mathrm{d}x)$ (Schultz & Flack 2007) remains below $K \leqslant 1.56 \times 10^{-9}$ along the domain of interest (i.e. DNS domain), confirming that the external flow conditions approximate ZPG. In the previous definition, the external velocity (U_e) is retrieved

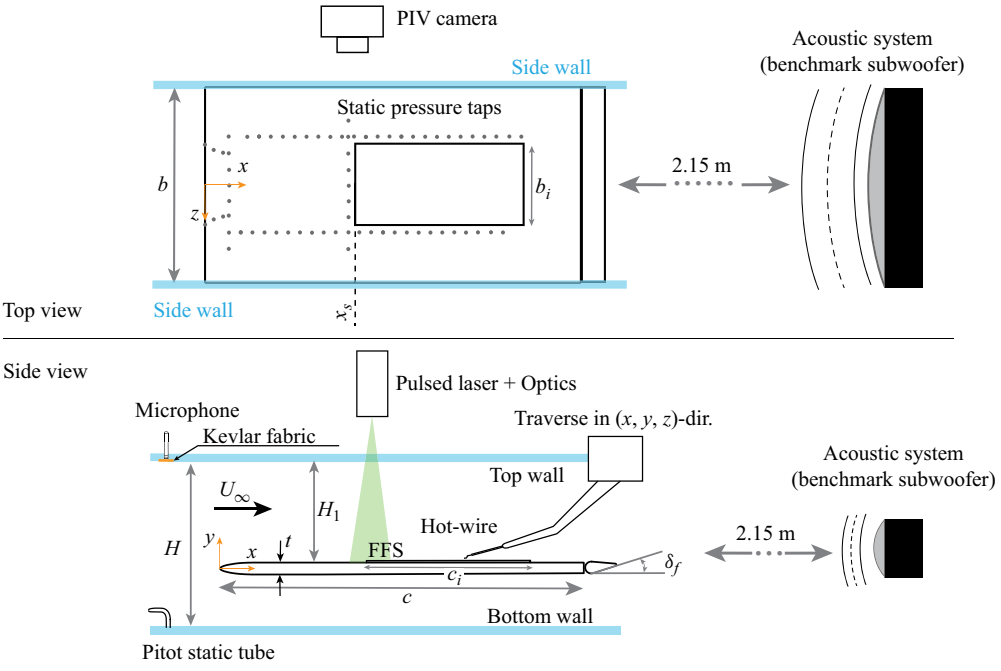

Figure 2. Diagram of the experimental set-up showing the unswept flat plate, the FFS insert, the acoustic forcing system and the arrangement of the different flow measurement techniques used.

from the static pressure tap measurements (custom-made pressure scanner equipped with Honeywell HSC series differential pressure transducers), assuming that $\partial p/\partial y = 0$. The pressure taps' approximate location is sketched in figure 2. Pressure measurements close to the LE monitor the stagnation point location, while the spanwise and streamwise distributed pressure readings allow for verification of the 2-D flow assumption (see pressure tap measurements at $z = \pm 120$ mm from the midspan in figure 5*a*). Finally, the reference velocity (U_0, see table 1) is determined from the static pressure averaged across two rows of pressure taps at $z = \pm 120$ mm (see grey solid line in figure 5*a*), measured at $x^* = (x - x_s)/\delta_0^* = -193$ (see black marker in figure 5*a*).

The machined aluminium plate features an average surface roughness lower than $R_a \approx 0.3\,\mu$m (with $R_q \leqslant 0.4\,\mu$m and $R_z \leqslant 4\,\mu$m) and a modified super ellipse (MSE) geometry at the LE with an aspect ratio of 6. This design moves the suction peak towards the LE and reduces the adverse pressure gradient around the LE region (Lin, Reed & Saric 1992), ensuring a rapid development towards a nominal Blasius boundary layer. The stagnation point and the LE pressure distribution are further adjusted with a 50 mm trailing-edge flap deflected approximately 33° upwards. The latter ensures that the stagnation point is located on the upper side of the plate, avoiding unsteady separation effects. The flow on the bottom side (non-measuring side) is forced to turbulence with zig–zag tape to avoid flow separation at the trailing edge. The zig–zag tape was placed 50 mm downstream of the LE (i.e. $x^* \approx -355$).

2.2.1. *Modelling and characterisation of the step geometry*

The flat-plate model used in this experiment features a rectangular cavity that spans 380 mm $\leqslant x \leqslant$ 808 mm in the streamwise direction and -104 mm $\leqslant z \leqslant 104$ mm in the spanwise direction (see geometry in figure 2 and dimensions in table 2). In this work,

c	b	H	t	H_1	c_i	b_i	x_s	δ_f
0.95 m	0.5 m	0.5 m	20 mm	0.35 m	0.428 m	0.208 m	0.38 m	33 deg

Table 2. Geometric parameters of the unswept flat-plate model. Parameters are indicated in the schematic in figure 2.

an insert is placed inside the cavity to simulate steps. A precision linear translation mechanism on the rear side of the model insert enables creating both backward- and forward-facing steps. The step height at the model-insert intersection ($x_s = 0.38$ or $x_s^* = 0$) can be adjusted.

Finally, step heights are characterised using a Micro-Epsilon 3010–25BL laser scanner (resolution of 1.5 µm) that is traversed along the span ($-80\,\text{mm} \leqslant z \leqslant 80\,\text{mm}$) at the step location. The average step height along the span ($\overline{h}$) and the step spanwise uniformity (standard deviation of h, $\sigma_{\overline{h}}$) are specified in table 1. While utmost care was taken in the fabrication and assembly of the step insert, the laser scan characterisation revealed a narrow and deep ($w/d \ll 1$) gap of width $w = 320\,\mu\text{m}$ ($w/\delta_0^* = 0.34$) at the intersection between the flat plate and the step insert. Due to the inherent pressure difference between the two sides of the flat plate, a weak suction flow forms at this gap. This residual suction at $x^* \approx 0$ had a weak stabilising effect on the TS waves. Thus, to ensure consistency between experimental and DNS results, this localised suction region in front of the step is also reproduced in the DNS, as later detailed in § 2.3.1.

2.2.2. *Acoustic forcing of TS waves*

Similar to the experiments of Saric, Wei & Rasmussen (1995), this work leverages the receptivity of LE roughness to acoustic pressure fluctuations to force single-frequency TS waves at $f = 450$ Hz ($F = 90$). A 120 W benchmark speaker located 2.15 m downstream of the LE (see figure 2) generates a deterministic plane acoustic wave at the desired forcing frequency. The acoustic wave amplitude and frequency are monitored using a GRAS 46BE analogue free-field microphone flush mounted on the top wall of the test section; see figure 2. In addition, Kevlar type 120 fabric covers the side of the microphone facing the flow to reduce the permeability to hydrodynamic fluctuations with respect to sound waves. The sound pressure level recorded under acoustic forcing was kept below 80 dB (band-pass filtered between $20\,\text{Hz} \leqslant f_{bp} \leqslant 20\,\text{kHz}$) to prevent nonlinear receptivity (Saric *et al.* 1995; Placidi, Gaster & Atkin 2020).

The model's MSE LE design eliminates the curvature discontinuity between the flat plate and LE juncture, ensuring receptivity only at the nose of the LE (Lin *et al.* 1992). To verify the efficacy of the acoustic forcing towards generating monochromatic TS waves, the coherence between the pressure and velocity signals measured by the microphone and hot wire, respectively, was assessed. The results revealed strong coherence between both signals at the acoustic forcing frequency, i.e. $f_{ac} \simeq f_{TS}$.

The driving voltage of the speaker is adjusted according to the desired TS wave amplitude, which is recorded at $x^* = -43$ (P1 in figure 3) in baseline conditions with a hot wire. The choice for TS wave amplitude during the experiments is made on the basis of the expected interaction dynamics at the vicinity of the step. More specifically, the acoustic forcing amplitude is chosen such that there is a linear development of the perturbation in both baseline and step conditions, as well as a high hot-wire signal-to-noise ratio for the forced TS mode compared with natural TS waves. Herein, natural TS waves denote disturbances triggered by the background noise of the wind tunnel,

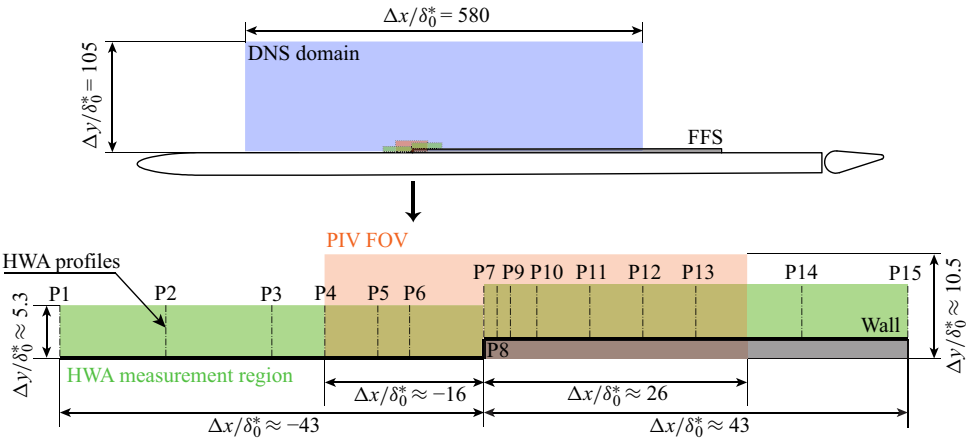

Figure 3. Location and dimension of PIV field of view (FOV, orange), HWA measurement region (green) and DNS domain (blue) within the flat-plate set-up. The dimensions of the measurement regions are drawn to scale with the flat-plate cross-section dimensions. The DNS domain starts at $x^* = -247$.

i.e. without acoustic forcing. The final TS amplitude under continuous acoustic forcing at $F = 90$ was $A/U_0 \approx 0.17\,\%$ (corresponding to $A^{rms}/U_0 \approx 0.12\,\%$); see table 1. This is obtained from the amplitude of the fast Fourier transform (FFT) of the hot-wire signal at $F = 90$, evaluated at the y coordinate where A is maximum. Additionally, the spanwise uniformity of the forced TS wave is assessed by comparing the TS amplitude and shape at two additional spanwise stations, specifically at $z/\delta_0^* = -11$ and $z/\delta_0^* = 11$, using PIV. The relatively small differences in amplitude ($\Delta A/A \leqslant 3.2\,\%$) confirm the two-dimensionality of the forced TS wave.

An immediate consequence of an acoustic wave travelling across a boundary layer is the formation of a Stokes layer (SL, Placidi *et al.* 2020), as described in Stokes' second problem (Batchelor 2000). Since the TS wave and the SL share the same frequency, it is challenging to experimentally separate one from the other, as observed in the experiments of Saric *et al.* (1995). To address this challenge, White, Saric & Radeztsky (2000) proposed a technique that leverages the differences in phase speeds between the TS wave and SL. This technique involved the use of a sinusoidal pulse with frequency f_{pulse}, rather than a continuous acoustic signal in time. Since TS waves travel at a much lower phase speed than the SL, their signal on the hot wire appeared delayed compared with the SL.

The approach of White *et al.* (2000) was implemented in these experiments using PIV to evaluate the influence of the SL on the measurements performed with a continuous acoustic signal. The TS wave amplitude measured at the start of the PIV domain (see figure 3) under both pulsed and continuous forcing revealed no significant difference, with a maximum deviation of $\Delta A/A \leqslant 2\,\%$. The influence of the SL on the TS wave amplitude measurements can be significant in receptivity studies, where the amplitude of the TS wave is of a similar magnitude to that of the SL (Chauvat 2020). However, in the context of the present experiments, where the measurement region is located within the exponential growth regime of TS waves, the amplitude of the SL was considerably smaller than that of the forced TS wave. Considering this, a continuous acoustic forcing is used to excite TS waves during the experiments presented in this work. The effect of the SL is hereinafter considered negligible.

It is important to note that under these conditions, local receptivity to acoustic forcing at the sharp FFS edge can be plausibly expected to play a role in the dynamics of the

developing flow. Nevertheless, as later shown in this work, the good agreement between the DNS (which did not employ acoustic forcing) and the experiments (with acoustic forcing), both in terms of perturbation growth and shape, indicates that any acoustic receptivity at the FFS edge, if present, does not significantly influence the downstream perturbation dynamics.

2.2.3. *Hot-wire anemometry*

Hot-wire anemometry measurements are conducted to examine the temporal dynamics of the perturbation field in proximity to the FFS. The HWA set-up consists of a single-wire boundary-layer probe (Dantec Dynamics 55P15) operated by a TSI IFA-300 constant temperature bridge. The HWA voltage signal is converted into velocity using an *in-situ* calibration with corrections for changes in ambient temperature, following the procedure described in Hultmark & Smits (2010). In addition, an automated three degrees-of-freedom traverse system is employed to position the HWA probe, with a step resolution of 2.5 μm and a positional accuracy of 10 μm in all directions.

Fifteen boundary-layer profiles are measured at the model's midspan, within a streamwise region covering 40 mm upstream and 40 mm downstream of the step location (i.e. $-43 \leqslant x^* \leqslant 43$); see figure 3. The streamwise spacing between successive boundary-layer profiles is reduced from 10 to 1.25 mm immediately downstream of the FFS to capture the complex flow dynamics reported in this region (Edelmann 2014). Each boundary-layer profile consists of 60 measurement points logarithmically distributed in the wall-normal direction to increase the spatial resolution near the wall ($\Delta y_{min}/\delta_0^* = 0.01$ and $\Delta y_{max}/\delta_0^* = 0.33$). The logarithmic spacing conveniently yields a higher resolution around the TS maxima and around regions of high shear downstream of the FFS edge. The HWA sampling frequency is set to $f_s = 51.2$ kHz, with the acquisition system featuring an anti-aliasing filter at $0.45 f_s$. The total measuring time per point is set to 3 s to ensure statistical convergence of first- and second-order statistics. The dynamic response of the HWA system was evaluated *a posteriori* using a square-wave test, yielding a frequency response of 17 kHz.

The boundary-layer profiles are acquired by placing the probe in the free stream and approaching it to the wall until the measured velocity is 10 % of the external velocity, U_e. In addition, the wall distance of the last measurement point near the wall is monitored using a Taylor–Hobson micro-alignment telescope (resolution of 20 μm). A final adjustment of the wall distance is done by matching the experimental profiles to the corresponding numerical profiles extracted from DNS.

The perturbation field is obtained by subtracting the time-averaged velocity ($\overline{U}(x, y)$) from the instantaneous velocity ($U(x, y, t)$) signal at each point as

$$u(x, y, t) = U(x, y, t) - \overline{U}(x, y). \tag{2.1}$$

The hot wire is most sensitive to the velocity components perpendicular to the sensor. In these experiments, the wire is placed parallel to the flat-plate LE, rendering the probe sensitive to streamwise and wall-normal velocity components, namely $Q + q = [U + u, V + v]$. However, since V is usually small compared with U ($V = O(1/Re)$), the resultant velocity can be approximated by the streamwise-velocity component, i.e. $Q \approx U$. Similarly, since u is superposed on U, the fluctuating part measured by the hot wire can be approximated as $q \approx u$ (Saric *et al.* 2007). Note that this assumption becomes less sound for HWA profiles close to the step region, where the flow is deflected in the wall-normal direction, with V being of the order or larger than U close to the FFS edge (see results in § 3). However, given the good agreement between HWA and DNS U-velocity

profiles (see § 3), and for consistency with previous studies using HWA for TS wave boundary-layer measurements (e.g. Downs & Fransson 2014), $Q + q \approx U + u$ is assumed for subsequent comparison of HWA with DNS in regions sufficiently far from the step.

2.2.4. *Planar PIV*

Planar PIV (two-component two-dimensional PIV) measurements are conducted to characterise the mean flow distortion and perturbation field topology across the FFS. The field of view (FOV) around the step spans $-16 \leqslant x^* \leqslant 26$ at the model's midspan ($z = 0$). Figure 3 presents the PIV FOV dimensions compared with the HWA measurement region.

A Quantel Evergreen dual-pulse Nd:YAG laser (200 mJ per pulse) is used to illuminate micron-sized tracer particles during a very short pulse duration ($\Delta t_{pulse} \leqslant 10$ ns) with a monochromatic light beam, $\lambda = 532$ nm (green light). Water-glycol tracer particles (average diameter of 1 µm) are injected in the wind tunnel stream.

Images of the illuminated seeded airflow are captured by a LaVision Imager sCMOS camera (2560 × 2160 pixels, 16 bit and 6.5 × 6.5 µm^2 pixel size) positioned outside the test section and orthogonal to the laser light sheet. To characterise in detail the boundary-layer flow, the camera is fitted with a $f = 200$ mm lens operated at an optical aperture of $f_\# = 11$, leading to a high magnification factor of $M = 0.4$ and a spatial resolution of 15.6 µm px^{-1}. Image pairs are recorded at an inter-frame time of $\Delta t = 19$ µs such that the maximum particle displacement in the free-stream region is roughly 25 pixels. Accounting for a typical uncertainty on the particle image displacement of 0.1 pixels (Sciacchitano, Scarano & Wieneke 2012), the minimum velocity that can be measured is $\min(|U|) \approx 0.08$ m s^{-1}, yielding a dynamic velocity range of 200.

The laser and camera are synchronised using a LaVision Davis Programmable Unit PTU X. Additionally, PIV acquisition and acoustic forcing are synchronised to realise phase locking of the PIV measurements in reference to the forced TS wave. Image pairs are captured at a frequency rate of 15 Hz. In this work, high-resolution phase locking is achieved by setting a small phase increment between successive image pairs ($\Delta\phi = 5\pi/180$ rad), acquiring 72 phases within the TS cycle. The resulting dataset consists of 1944 images, which are used to compute statistical quantities of the flow and perform a temporal FFT analysis (see, e.g. TS amplitude and phase from PIV results in figures 7 and 8). Although each phase is represented by a relatively low number of images (27 frames per phase), this number is deemed sufficient for the qualitative comparisons made between DNS and PIV data presented in § 4.1. Later post-processing of the images is performed using LaVision Davis 10.2 software, where the final interrogation windows are set to 12 × 12 px with 75 % overlap after applying a multi-stage cross-correlation. The highest uncertainty in the time-averaged velocity field is found downstream of the FFS edge, in a region where the DNS results exhibit strong velocity gradients. In this region, the maximum uncertainty on $\overline{U}$ remains below $\varepsilon_{\overline{U}}/U_0 \leqslant 0.3$ %.

2.3. *Numerical set-up*

2.3.1. *Direct numerical simulations*

Direct numerical simulations are performed at DLR using the Nek5000 code (Fischer, Lottes & Kerkemeier 2008), which solves the incompressible Navier–Stokes equations. The Nek5000 code employs the spectral element method (SEM), where the physical domain is decomposed into spectral elements. Within each element, the flow field solution is represented as a sum of Lagrange interpolants, defined on an orthogonal basis of Legendre polynomials up to degree p. The simulations presented in this study are conducted with a polynomial order of $p = 9$, and grid convergence is verified using $p = 11$.

As the focus of this work is on 2-D TS waves, the DNS simulations are restricted to 2-D domains (see figure 3).

Initially, a DNS of the laminar 2-D base flow is performed. For this purpose, inflow velocity profiles (i.e. U_{BL} and V_{BL}) are prescribed at $x^* = -247$, obtained as a solution of the boundary-layer equations, using the measured external velocity $U_e(x)$ as the boundary condition. The outflow boundary condition is specified as $\partial V/\partial x = 0$ and $Re^{-1}(\partial U/\partial x) - p = -p_a$, where $p_a = -Re^{-1}(\partial U_{BL}/\partial x)$ represents an ambient pressure. On the free-stream boundary, a modified stress-free condition is applied: $U = U_e(x)$ and $Re^{-1}(\partial V/\partial y) - p = -p_b$, where $p_b = \hat{p} - Re^{-1}(\partial V_{BL}/\partial y)$. Here, $\hat{p}$ is obtained by substituting the velocity profiles derived from the boundary-layer solution into the Bernoulli equation. At the wall, the standard no-slip condition is modified to account for the narrow and deep gap at the intersection of the flat plate and the step insert, as described in § 2.2.1. This gap, characterised by a width of $w = 320\,\mu\text{m}$ ($w/\delta_0^* = 0.34$), induces a localised suction effect with a measured wall-normal velocity component of approximately $V_s/U_0 \approx -0.01$, as confirmed by PIV measurements under baseline conditions. To replicate the influence of this suction effect on the incoming disturbances, the gap itself is not explicitly meshed in the DNS. This decision is supported by the experimental findings of Crouch *et al.* (2022), who demonstrated that the effect of deep surface gaps on TS-dominated laminar-to-turbulent transition can be approximated by $\Delta N \approx 0.1 w/\delta^*$. For the present conditions, this yields a negligible transition shift of $\Delta N = 0.034$. Instead, the induced localised suction effect is modelled by imposing a non-zero wall-normal velocity component. The suction profile is defined using a hyperbolic tangent function, which avoids strong gradients at the boundaries of the gap ($-0.34 \leqslant x^* \leqslant 0$) and remains nearly constant in the middle region of the gap. The imposed maximum suction velocity ($V_s/U_0 \approx -0.01$) aligns with the experimental measurement. By incorporating this localised suction effect into the simulation, the DNS set-up aims to closely reconstruct the experimental baseline conditions, facilitating meaningful comparisons between the numerical and experimental results, as further detailed in § 4.

The steady solution obtained after the initial transient has subsided represents the 2-D base flow. Subsequently, a simulation is conducted in which unsteady disturbances are superimposed on the base flow. To introduce periodic TS waves, a time-harmonic blowing and suction strip, centred at $x^* = -193$, is applied at the wall. The normal velocity is prescribed across the strip as $V(x, t) = A_{2D} f(x) \sin(\omega t)$, where ω is the circular frequency of the fundamental TS mode and $f(x)$ is a shape function designed to ensure zero net volume flow through the strip and to provide smooth derivatives near its start and end points. The amplitude A_{2D} is chosen such that the developing TS wave matches the amplitude measured with HWA at $x^* = -43$. To prevent numerical instabilities at the outflow boundary, a sponge region is implemented to smoothly damp perturbations. After the initial transient caused by the introduction of disturbances has vanished, the DNS solution is Fourier analysed in time to extract the fundamental TS mode.

2.3.2. *Boundary-layer stability*

A comparison between the DNS solution and predictions from LST provides valuable insights into the perturbation characteristics under FFS conditions, as demonstrated in § 5.1. In this study, two distinct linear stability formulations, namely the OS equations (Orr 1907; Sommerfeld 1909) and the linear parabolised stability equations (LPSE) (Herbert 1997) are employed, using the DNS base flow as input.

The OS and LPSE stability analyses are conducted on a Cartesian grid featuring a uniform spacing ($\Delta x^* = 19.4 \times 10^{-2}$) in the x direction and pseudo-spectral discretisation

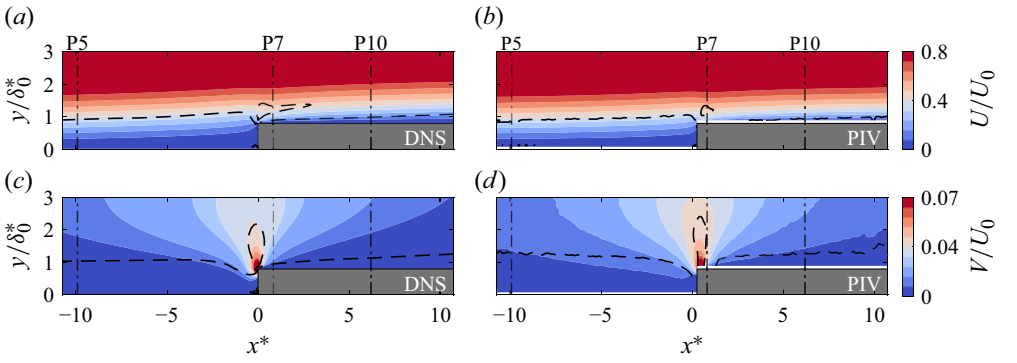

Figure 4. Contours of the mean flow velocity components (U and V) from DNS (*a*,*c*) and PIV (*b*,*d*), where $x^* = (x - x_s)/\delta_0^*$. Inflection points of U and V, $\partial^2 U/\partial y^2 = 0$ (*a*,*b*) and $\partial^2 V/\partial y^2 = 0$ (*c*,*d*), are indicated in black dashed lines (- - -). Vertical dash-dotted black lines indicate the streamwise locations of HWA profiles P5, P7 and P10.

in the wall-normal direction by means of $n_y = 80$ Chebyshev polynomials. The derivatives in the wall-normal direction are approximated using pseudo-spectral Chebyshev differentiation matrices. In the particular case of LPSE, the derivatives in the streamwise direction are approximated using a first-order backward Euler (explicit) scheme. Further details on the LPSE and OS solver's numerical implementation can be found in Westerbeek (2020).

3. Effect on mean flow

This section evaluates the mean flow modification caused by the presence of a FFS under the flow conditions presented in table 1. Figure 4 shows the contours of the streamwise and wall-normal velocity components, as obtained from PIV and DNS results. To facilitate a direct comparison between DNS and PIV mean flow results, the DNS mean flow is defined as

$$Q_{mean\ flow} = Q_{base\ flow} + q_{(0,0)}, \tag{3.1}$$

where $q_{(0,0)}$ denotes the mean flow deformation resulting from the (weak) nonlinear interaction of the primary TS wave and its harmonics. The comparison of DNS and PIV mean flow fields in figure 4 shows overall good agreement. Notably, PIV also captures the abrupt increase in V near the step edge.

The pressure coefficient over the flat plate is shown in figure 5(*a*), with a zoomed view around the step shown in figure 5(*b*). The pressure imposed in the DNS at the top boundary condition is set to match the pressure measured at the wall during experiments in baseline conditions (i.e. grey solid line in figure 5*a*). Given that the pressure exhibits a weak variation in the wall-normal direction ($\partial p/\partial y \approx 0$), differences between pressure tap readings (symbols in figure 5*a*–*b*) and DNS wall pressure (orange solid line in figure 5*b*) are negligible. Note that the small jump in pressure observed in figure 5(*b*) is due to the simulated suction slot upstream of the FFS. The pressure coefficient at the wall in step conditions could not be measured during the experiments since the available pressure taps were located outside of the step insert (see figure 2).

The boundary layer is subject to a progressively growing adverse pressure gradient as it approaches the step (figure 5*b*). Regions of low-momentum fluid near the wall are subject to large curvature ($\partial^2 U/\partial y^2$) changes due to the pressure gradient (Stratford 1959). This creates an inflection point that moves away from the wall with an increasing

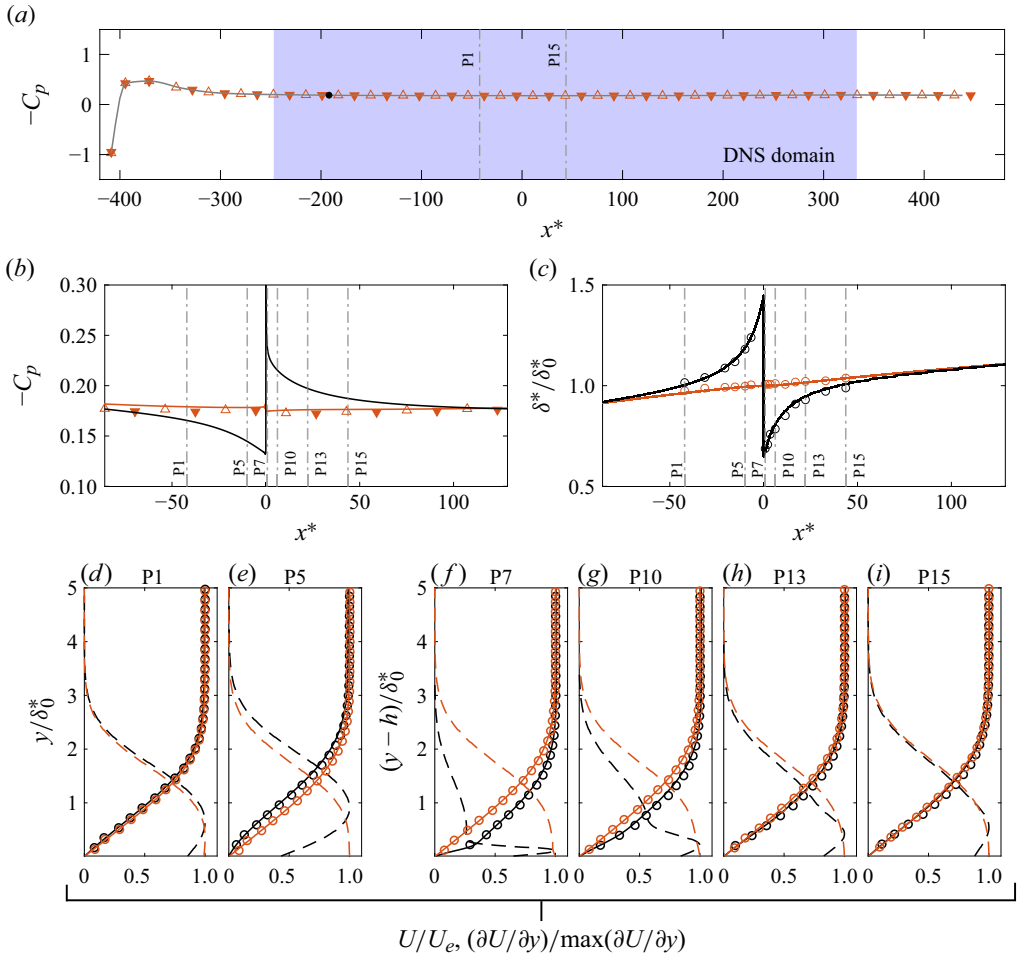

Figure 5. (*a*) Pressure coefficient ($-C_p$) from tap readings at two different spanwise locations, left ($z = -120$ mm, ▼) and right ($z = 120$ mm, △) of the midspan (see figure 2). The average between left and right pressure taps is represented by a solid grey line (——). The blue area represents the spanwise extent of the DNS domain, whereas vertical dashed lines delimit the HWA domain. The streamwise location used for measuring the reference velocity is indicated by a black marker (●). (*b*) Pressure coefficient, $-C_p$, from pressure tap measurements (symbols) and from DNS results at the wall in both baseline (——) and FFS conditions (——). (*c*) Displacement thickness, δ^*, and (*d–i*) boundary-layer velocity profiles ($U(y)$, ——) and mean shear profiles ($\partial U/\partial y$, - - -) in FFS (black) and baseline (orange) conditions. In figures (*c–i*), symbols (○) denote experimental HWA data and solid lines (——) DNS. Streamwise location of profiles shown in (*d–i*) are indicated by vertical dash-dotted grey lines (-·-·-) in (*b*) and (*c*). The HWA velocity profiles from (*d*,*e*) are located upstream of the FFS, while profiles from (*f–i*) are located downstream. Refer to table 3 for the corresponding streamwise location (x^*) of each profile.

adverse pressure gradient, as shown by the dashed black lines in figure 4(*a*,*b*). The loss of streamwise momentum close to the wall leads to an expansion of the boundary layer in the wall-normal direction (see figure 5*e*), increasing its displacement thickness, as shown in figure 5(*c*). Similar observations are reported in the DNS base flow results of Edelmann (2014) upstream of the smallest FFS simulated, i.e. $h/\delta^* = 1$ and $Re_h = 1000$ in figure 1(*a*).

The weak local suction in front of the step interrupts the otherwise present recirculating region developing upstream of the FFS, which becomes hardly noticeable either from PIV or DNS mean flow fields presented in figure 4. Downstream of the FFS, no secondary

P1	P2	P3	P4	P5	P6	P7	P8	P9	P10	P11	P12	P13	P14	P15
−42.10	−31.37	−20.64	−15.28	−9.91	−6.69	0.82	2.16	3.50	6.18	11.54	16.91	22.27	33.00	43.73

Table 3. Streamwise location ($x^* = (x - x_s)/\delta_0^*$) of HWA profiles indicated in figure 3.

recirculating region is observed from DNS results. This observation is independent of the presence of the upstream weak local suction and is in line with previous numerical works performed under similar free-stream conditions and using similar FFS configurations (e.g. works by Edelmann 2014 and Teng 2023, indicated in figure 1*a*).

Figure 5(*b*) shows a sharp increase in pressure at the FFS edge, followed by a more gradual pressure decrease until baseline values are reached. In line with the observations of Eppink (2020) for three-dimensional boundary-layer transition, governed by S-CFI, figure 4(*a*,*b*) shows a kink in U, concurrent with the rapid growth in V at the FFS. Eppink (2020) attributes this behaviour to the strong displacement of wall-normal momentum away from the wall (see figure 4*c*,*d*) which needs to be compensated by an also high streamwise momentum injected close to the wall to satisfy mass conservation.

The displacement thickness suddenly decreases due to the strong favourable pressure gradient, but smoothly recovers to baseline values downstream, as shown in figure 5(*c*). The HWA velocity profiles downstream of the FFS edge (figure 5*f*–*i*) provide further insight into boundary-layer modifications due to the abrupt pressure changes at the FFS edge. Downstream of the FFS, the boundary layer attains a dual structure characterised by two different maxima in $\partial U/\partial y$, which can also be observed from the contour lines in figure 4(*a*,*b*). This modular composition of the boundary layer is the result of the curvature change undergone due to the presence of two quasi-simultaneous opposite pressure gradients. It would appear that the effect of such a strong and delimited favourable pressure gradient persists downstream of the FFS (figure 5*g*), imprinted in the boundary-layer curvature. Further downstream ($x^* \geqslant 22$), this effect is suppressed and the adverse pressure gradient prevails. This modification is evident from the merging of the two $\partial U/\partial y$ peaks in figure 5(*h*,*i*) and the dashed black lines in the contours of figure 4(*a*,*b*), which indicate the boundary-layer inflection points.

4. Effect on TS wave development

The results presented in the previous section reveal abrupt and spatially confined distortions of the mean flow in close proximity to the step. While the distortion experienced by the mean flow upstream of the step can be widely encountered in a number of well-documented stability problems, e.g. upstream of laminar separation bubbles (Marxen, Lang & Rist 2012) or in front of smooth roughness elements (Park & Park 2013), and it is well known to effectively destabilise TS waves. However, compared with the upstream mean flow distortion, the type of mean flow distortion observed downstream of the step has not been widely studied in the literature. It is therefore necessary to evaluate the effect of such modulation on the overall boundary-layer stability.

This section will study the effect of the step on the growth of the fundamental TS wave mode at $F = 90$ (table 1). Both experimental and DNS data will be used to this goal.

4.1. *Fundamental mode amplitude and phase*

The development of the fundamental mode's streamwise-velocity perturbation amplitude ($A^{\tilde{u}}$) in step and baseline conditions is shown in figure 6(*a*), as obtained from HWA

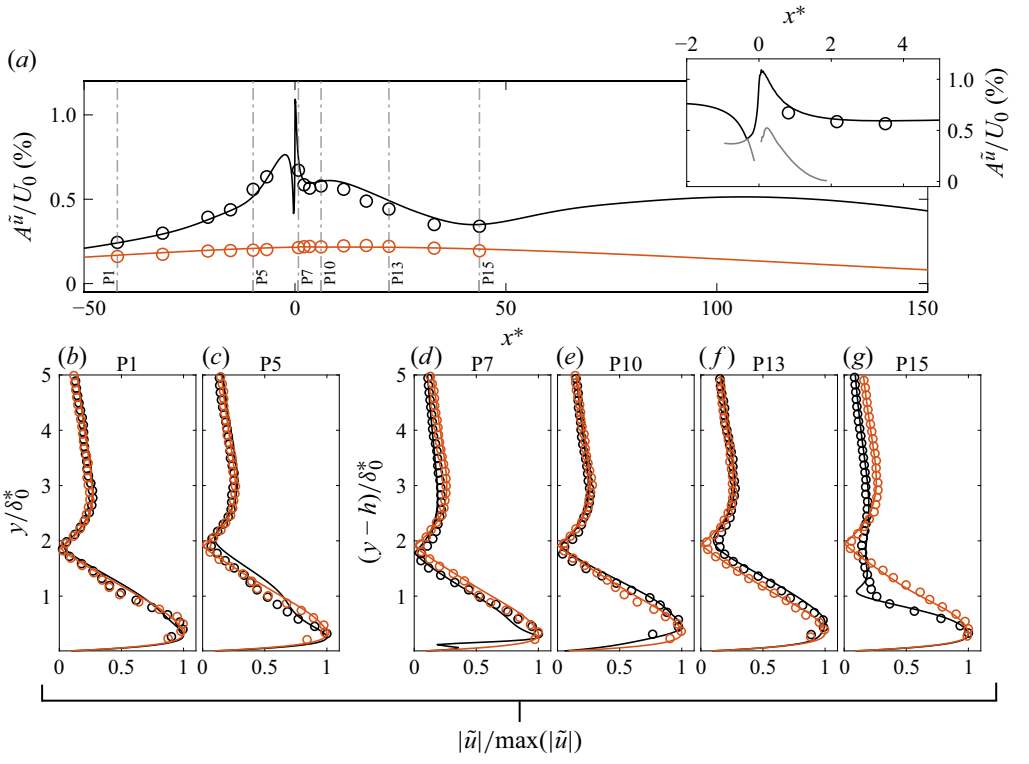

Figure 6. (*a*) The amplitude of the fundamental TS mode and zoomed view close to the step vicinity from HWA measurements (○) and DNS (——). Grey solid lines in the zoomed figure correspond to the amplitude of the near-wall peak emerging in the perturbation profile close to the step. (*b–g*) The TS wave perturbation profile upstream (*b*,*c*) and downstream (*d–g*) of the FFS. Refer to table 3 for the corresponding streamwise location (x^*) of each profile. Results in FFS conditions are indicated in black (——) and in baseline conditions in orange (——). Streamwise location of profiles shown in (*b–g*) are indicated by vertical grey dash-dotted lines (-·-·-) in (*a*).

measurements and DNS. Similarly, the u-perturbation profiles measured at six streamwise stations in the vicinity of the step are presented in figure 6(*b–g*). In figure 6(*a*), $A^{\tilde{u}}$ is retrieved at the wall-normal location where $|\tilde{u}|$ (shown in figure 6*b–g*) becomes maximum. Excellent agreement is observed between DNS and HWA results in terms of TS amplification and u-perturbation shape. Despite HWA measurements not being able to capture the secondary near-wall lobe emerging downstream of the step (see DNS solution in figure 6*d*), they accurately capture the highly distorted TS perturbation profile at P15 (see figure 6*g*). The excellent agreement between experiments and DNS is further confirmed when comparing the spatial distribution of streamwise-velocity perturbation amplitude ($|\tilde{u}|$, figure 7*a–c*) and phase ($\varphi^{\tilde{u}}$, figure 8*b*,*c*,*e*) obtained from DNS and PIV measurements, e.g. compare figures 7(*a*,*b*) and 8(*b*,*c*).

Figure 6 shows exponential growth of the fundamental mode's amplitude upstream of the FFS, following the progressive pressure increase (note C_p curve in figure 5*b*). In this region upstream of the step ($-15 \leqslant x^* \leqslant 0$), the TS shape exhibits an increase in perturbation amplitude at a higher wall-normal location (note thickening of the TS wave shape in figure 7*c* around $y/\delta_0^* \approx 1$), which coincides with a region where the mean shear is maximum (note the mean shear profiles in figure 5*d*,*e* around $y/\delta_0^* \approx 1$ and black dashed line in figure 7, indicating the inflection points). This is a well-known behaviour observed

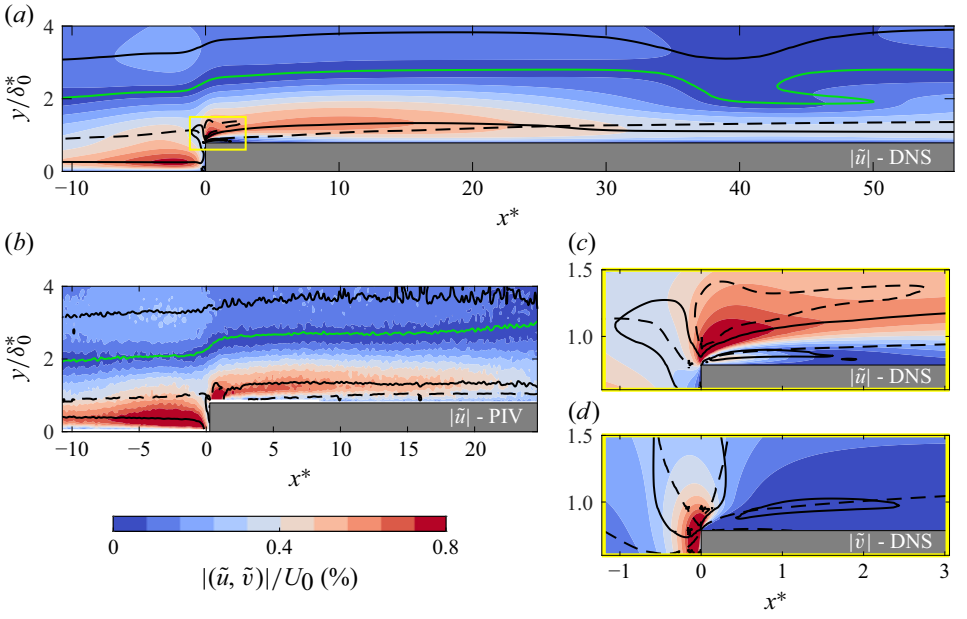

Figure 7. Contours of the perturbation velocity ($\tilde{u}$ and $\tilde{v}$) from DNS (*a*,*c*,*d*) and PIV (*b*) in FFS conditions. Subfigures (*c*,*d*) constitute contours of streamwise (*c*) and wall-normal (*d*) perturbation velocity in a zoomed region delimited by a yellow box in (*a*) around the step corner. Solid lines denote the maxima (——) and minima (——) in the TS shape profile for $|\tilde{u}|$ (*a*–*c*) and $|\tilde{v}|$ (*d*). Dashed lines (- - -) indicate the inflection points in U (*a*–*c*) and V (*d*).

in TS waves when entering regions of strong adverse pressure gradients, like a laminar separation bubble (see, e.g. figure 17 in Dovgal, Kozlov & Michalke 1994) or upstream of a 2-D hump (see, e.g. figure 10 in Park & Park 2013).

Immediately upstream of the step ($-1 \leqslant x^* \leqslant 0$), the distortion induced by the FFS on the TS instability results in a substantial transfer of streamwise perturbation momentum in the wall-normal direction. This can be clearly distinguished by comparing the amplitude fields of $|\tilde{u}|$ (figure 7*c*) and $|\tilde{v}|$ (figure 7*d*), where $|\tilde{u}|$ decays upstream of the step, while $|\tilde{v}|$ is strongly amplified. This is also well observed from the growth rate results of $\tilde{u}$ and $\tilde{v}$ presented in figure 12(*b*) in § 5.2.

Immediately downstream of the FFS edge ($0 \leqslant x^* \leqslant 2$), a secondary peak develops in both $|\tilde{u}|$ and $|\tilde{v}|$ at the near-wall region (see black lines in figure 7*c*,*d* and near-wall region of the TS profile in figure 6*d*, i.e. $y/\delta_0^* \approx 0.2$). Similar observations are reported from the DNS results of Edelmann (2014) (see, e.g. figure 4.29 in Edelmann 2014). Interestingly, this feature occurs at a wall-normal location that coincides with a peak in the mean shear profile. This can be observed from the u-perturbation amplitude contours ($|\tilde{u}|$) close to the FFS in figure 7(*c*) (note dashed lines and full lines overlapping at $0.5 \leqslant x^* \leqslant 2$ and $y/\delta_0^* \approx 1$) and the near-wall peak emerging in the TS profiles, which also appears in the mean shear profile at the same streamwise station (see near-wall peaks in figures 5*f* and 6*d*). This peak in the mean shear was related in the previous section to the abrupt changeover from an adverse to favourable pressure gradient at the step. The amplitude of the near-wall $|\tilde{u}|$ peak decays in the streamwise direction (see grey lines in the inset of figure 6*a*), indicating that the feature giving rise to this peak disappears or merges with the original TS wave from $x^* \geqslant 2$. The perturbation phase (φ) contours of $\tilde{u}$ and $\tilde{v}$ in figures 8(*d*) and 8(*e*) reveal that this near-wall feature exhibits a phase shift with respect to

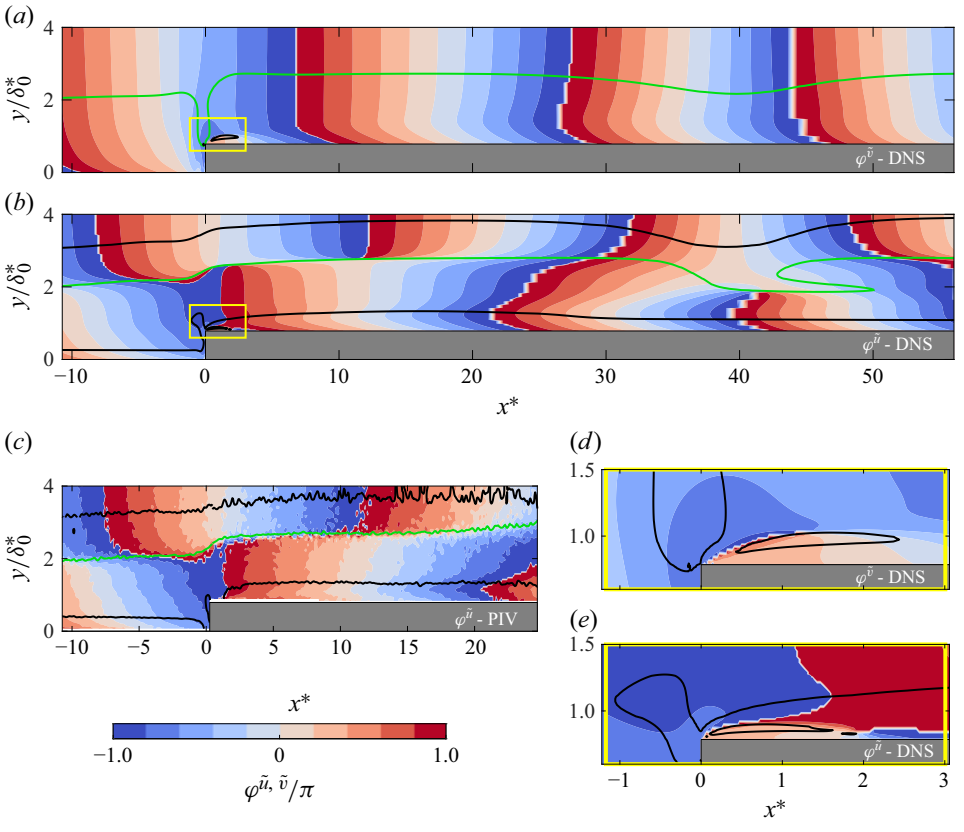

Figure 8. Contours of the streamwise ($\varphi^{\tilde{u}}$ in *b,c,e*) and wall-normal ($\varphi^{\tilde{v}}$ in *a* and *d*) perturbation phase from DNS (*a,b,d,e*) and PIV (*c*) in FFS conditions. Subfigures (*d,e*) constitute contours of the streamwise (*e*) and wall-normal (*d*) perturbation phase in a zoomed region delimited by a yellow box in (*a*) and (*b*) around the step corner. Solid lines denote the maxima (——) and minima (——) in the TS shape profile for $|\tilde{u}|$ (*b,c,e*) and $|\tilde{v}|$ (*a,d*).

the phase contours of the TS structure above. In the next section it will be shown that this phase shift between the incoming TS structure and the near-wall feature is related to their opposite signs in the perturbation streamfunction ($\mathrm{Re}(\psi)$, (4.1)).

Further downstream of the step ($x^* \geqslant 5$), the TS wave experiences a gradual stabilisation up to $x^* \approx 40$ (see figure 6*a*), followed by an inflection in growth and a prolonged destabilisation downstream up to $x^* \approx 100$, where it decays again, returning to the decaying trend observed in baseline conditions. The latter can be observed by comparing baseline and FFS case growth rates in figure 12, presented later in § 5.1. The decay-growth-decay-growth behaviour shown in figure 6(*a*) resembles the TS amplitude evolution reported in previous works downstream of isolated roughness or geometrical elements (e.g. Wu & Dong 2016 and Michelis *et al.* 2023*a*).

Interestingly, figure 6(*g*) shows an unconventional TS shape profile at P15 in FFS conditions. Both HWA and DNS capture a similarly distorted shape function. Further evidence of the substantial distortion undergone by the TS wave in this region ($20 \leqslant x^* \leqslant 60$) is found from the *u*-perturbation phase contours ($\varphi^{\tilde{u}}$) from DNS in figure 8(*b*). Unfortunately, the PIV domain does not extend sufficiently downstream to encompass the

region where the pronounced TS distortion occurs. Nevertheless, the agreement between the fundamental mode amplitude and phase contours from PIV and DNS elsewhere, coupled with the fact that the TS distortion is captured by HWA, points to the occurrence of this behaviour in the experiments. The topology of the TS wave in this region and the origin of this distortion are investigated in the following sections.

4.2. *Topology of the perturbation field*

The results presented in the previous subsection revealed two spatial regions where TS waves experience a strong distortion due to the presence of the step. First, a region in the vicinity of the FFS is found ($0 \leqslant x^* \leqslant 2$), where a near-wall velocity perturbation appears immediately downstream of the FFS edge. Second, a region further downstream of the FFS ($20 \leqslant x^* \leqslant 60$), where TS waves undergo a strong distortion in shape and phase, coinciding with local amplitude decay.

Figure 9 shows the perturbation structure around the FFS at three distinct phases within a TS period. In this study, the perturbation structure is visualised using isolines of the real part of the perturbation's streamfunction, ψ, which is defined as

$$u = \frac{\partial \psi}{\partial y} \quad \text{and} \quad v = -\frac{\partial \psi}{\partial x}, \tag{4.1}$$

where u and v denote the perturbation velocity components in the streamwise and wall-normal directions, respectively. These components are expressed as

$$\begin{bmatrix} u \\ v \end{bmatrix} = \begin{bmatrix} \tilde{u} \\ \tilde{v} \end{bmatrix} e^{-i\omega_0 t} + \text{c.c.}, \tag{4.2}$$

$$\tilde{u} = |\tilde{u}| e^{i\varphi^{\tilde{u}}}, \tag{4.3}$$

$$\tilde{v} = |\tilde{v}| e^{i\varphi^{\tilde{v}}}, \tag{4.4}$$

where c.c. denotes complex conjugate. The streamfunction ψ (4.1) is computed by integrating the perturbation field across the DNS domain using the trapezoidal rule.

In the vicinity of the FFS apex (see figure 9*b*,*d*,*f*), the perturbation exhibits a secondary structure featuring opposite sign in $\mathrm{Re}(\psi)$ with respect to the incoming TS wave (note the solid grey contour lines in figure 9*b*,*d*,*f*). According to the results presented in the previous section, this secondary feature manifests in the TS shape function as a near-wall peak (see figure 6*d*). The spatial region in which this near-wall structure is evident spans $0 \leqslant x^* \leqslant 2$, corresponding to about 11 % of the local TS wave streamwise wavelength ($\lambda_{TS}/\delta_0^* \approx 18$). The small dimension of this near-wall feature and its eventual decay (inset of figure 6*a*) in the streamwise direction (vanishing downstream, as observed in figure 9*b*,*d*,*f*) leads to a negligible effect on the incoming TS wave stability.

The flow features observed at the FFS edge for an incoming TS wave are notably similar to those in flows governed by a S-CFI. Casacuberta *et al.* (2022), studying the interaction between a FFS and S-CFI, report the presence of spanwise-distributed near-wall streaks emerging immediately downstream of the step edge and counter-rotating with respect to the incoming primary crossflow mode. The near-wall structures observed in Casacuberta *et al.* (2022) also arise at the FFS apex, at a near-wall region where the mean flow exhibits high wall-normal shears.

Casacuberta *et al.* (2025) attribute the onset of near-wall streaks to the lift-up effect, caused by the redistribution of streamwise momentum by the cross-stream perturbation components of the crossflow mode in regions of high wall-normal shear ($\partial U/\partial y$). The flow mechanism outlined in Casacuberta *et al.* (2025) can also explain the onset of the

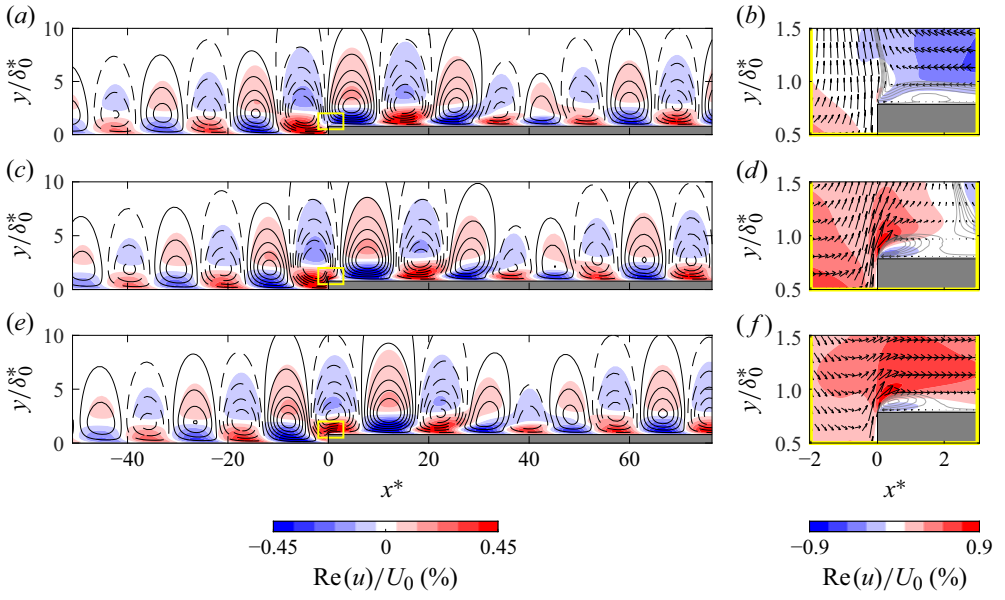

Figure 9. Real part of the streamwise-velocity perturbation component (contours) and isolines of the real part of the perturbation streamfunction (contour lines of Re(ψ), $-5.5\times10^{-6}\leqslant \mathrm{Re}(\psi)/(U_0\delta_0^*)\leqslant 5.5\times10^{-6}$) across different TS phases: $\phi=\pi/3$ rad (*a*,*b*), $\phi=2\pi/3$ rad (*c*,*d*) and $\phi=\pi$ rad (*e*,*f*). Zoomed-out FOV (*a*,*c*,*e*) and zoomed-in region at the step edge (*b*,*d*,*f*), bounded by a yellow box in the zoomed-out fields. Negative values of Re(ψ) are indicated with solid lines (——), whereas positive values of Re(ψ) are indicated with dashed lines (- - -). Grey solid contour lines in the zoomed-in region (*b*,*d*,*f*) constitute isolines of the perturbation streamfunction's real part (Re(ψ)), evaluated within the range $-2\times10^{-7}\leqslant \mathrm{Re}(\psi)/(U_0\delta_0^*)\leqslant 0$, and delineating the topology of the near-wall structure. Additionally, the spatial organisation of the perturbation velocity field is indicated by black quivers in (*b*,*d*,*f*). A video showing the evolution of the TS structure over the FFS for multiple phases (similar to *a*,*c* and *e*) is included as supplementary movie 1.

near-wall structure emerging at the FFS edge within a 2-D, time-periodic instability like the one concerned herein. At the FFS apex, the strong wall-normal perturbation velocity component ($\tilde{v}$, note length of velocity vectors in figure 9*d*), resulting from the incoming Re$(\psi)>0$ TS structure, displaces low-momentum fluid upwards in a region of high wall-normal shear ($\partial U/\partial y$), creating an instantaneous defect of streamwise perturbation velocity ($\tilde{u}$) near the wall (note blue contour in figure 9*d*, overlapping with ψ isolines of the near-wall structure). This u-defect region, elongated in the streamwise direction due to flow convection, eventually vanishes (see figure 9*b*,*d*,*f*) downstream as the peak in wall-normal shear weakens (see peak in $\partial U/\partial y$ profiles in figure 5*h*,*i*). When the incoming TS structure features negative Re(ψ) values, the opposite occurs, reversing the Re(ψ) sign of the near-wall structure. Interestingly, the mechanisms generating the near-wall feature in both TS–FFS interactions and in stationary CFI-FFS interactions involve the effective displacement of streamwise momentum by the cross-stream perturbation component (i.e. only v for the TS–FFS interaction) in a region of strong mean flow shear. For TS waves, this displacement is time dependent and shifts sign within the TS cycle, whereas for S-CFI, it is stationary and shifts sign along the spanwise direction, synchronous with the S-CFI wavelength, as reported by Casacuberta *et al.* (2025)

Downstream of the FFS edge ($20\leqslant x^*<60$), figure 9(*a*,*c*,*e*) shows a second region where the TS perturbation structure exhibits notable topological changes. In particular, the TS structure appears tilted in the mean shear ($\partial U/\partial y$) direction ($x^*\approx30$), gradually changing orientation towards a tilt against the mean shear ($x^*\approx50$), and recovering

further downstream to an upright orientation ($x^* \geqslant 60$), characteristic of the TS wave's asymptotic development. Notably, this region of topological changes in the perturbation structure coincides with a region where TS waves also exhibit an inversion in their growth trend (see figure 6*a*). The following section explores in more detail the instability mechanisms driving the observed tilting of the perturbation structure and consequent modifications in growth.

5. Mechanisms of flow instability near the step

The results presented in the previous sections reveal an excellent agreement between experimental and DNS results, leveraging confidence on the use of DNS results as a means to clarify the flow mechanisms driving TS–FFS interaction. Upstream of the step, TS waves follow exponential growth due to the FFS-induced adverse pressure gradient. In the FFS vicinity, both the mean flow and perturbation field undergo a spatially abrupt distortion, manifested by the emergence of a near-wall flow structure, locked at opposite phase and opposite perturbation streamfunction ($\mathrm{Re}(\psi)$) sign with respect to the incoming TS wave. Downstream of the step edge, the mean flow reverts to its canonical behaviour, while the perturbation field continues to display significant distortion, manifested by the tilting of the TS structure and a non-monotonic growth pattern (i.e. growth-decay-growth).

The nature of the perturbation behaviour observed downstream of the step remains unclear. This section aims to elucidate the stability characteristics (e.g. linear, nonlinear, parallel, local, etc.) of the perturbation field across the step to identify the stability mechanisms responsible for the observed TS modification.

5.1. *Linear, parallel and non-parallel stability characteristics*

The experiments and DNS performed in this work appear to capture the complete dynamics of the TS wave as it interacts with the step. However, towards elucidating the underlying mechanisms, it becomes instructive to leverage specific assumptions of flow linearity, parallelism and non-parallelism to isolate pertinent effects and reveal the relative influence on the complete perturbation behaviour. These assumptions are key for simplifications of the complete Navier–Stokes equations towards classical stability analysis methods such as LST and LPSE. Details on the numerical set-up employed to compute LPSE and LST are provided in § 2.3.2.

In practice, LPSE is typically used to avoid computationally expensive DNS simulations. However, since LPSE cannot march over the step (Tocci *et al.* 2021), where the highly non-parallel base flow invalidates PSE assumptions, an inflow condition is required downstream of the step. In the absence of more accurate solutions, this inflow is often set as a solution to the LST equations. Consequently, one possible scenario for the LPSE solutions downstream of the FFS would involve using a perturbation shape from LST as an inflow condition. This section compares two scenarios: LPSE results downstream of the step after initialisation with the perturbation profile from (i) DNS and (ii) the LST solution. Comparing these results, where DNS captures non-parallel effects that are not accounted for by LST, elucidates the importance of the upstream perturbation history in describing the TS wave distortion observed further downstream of the step. Table 4 summarises the different stability solutions studied.

To establish the DNS solution as the inflow for the LPSE when marching downstream of the step, it is necessary to compute the amplitude function and streamwise wavenumber of the fundamental mode from the DNS data. The streamwise wavenumber (α) is determined from the DNS solution by tracking the amplitude and the phase of the streamwise-velocity perturbation component (u) of the fundamental mode at the wall-normal location where

Identifier	Upstream solution ($x^* < 0$)	Inflow solution ($x^* = 6.4$)	Downstream solution ($x^* > 6.4$)
DNS	DNS	DNS	DNS
LST	LST	LST	LST
DNS-initialised LPSE	LPSE	DNS	LPSE
LST-initialised LPSE	LPSE	LST	LPSE

Table 4. Stability solutions studied in § 5.1.

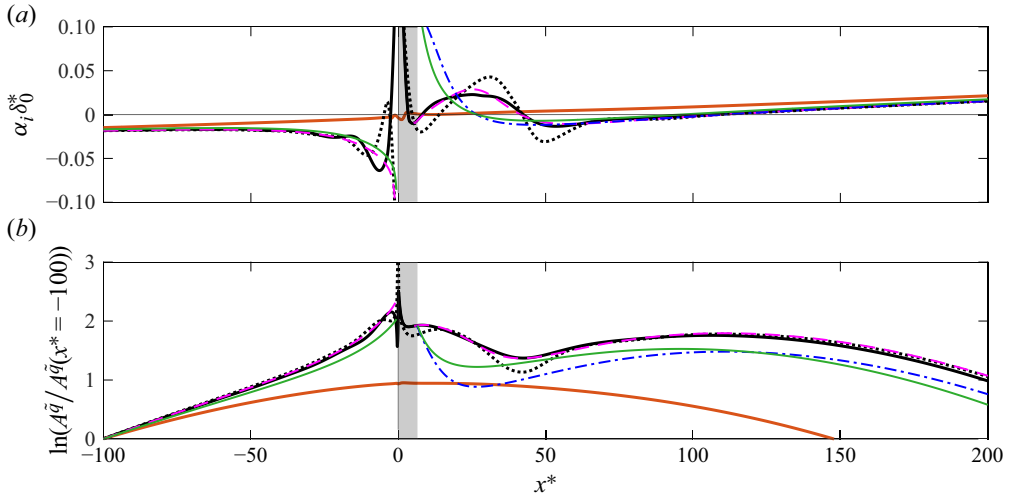

Figure 10. Growth rate (*a*) and *N* factor (*b*) as computed with DNS (——), DNS-initialised LPSE (- - -), LST (——) and LST-initialised LPSE (-·-·-) in FFS conditions. For the DNS solution, the growth rate and amplification of both $|\tilde{u}|$ (——) and $|\tilde{v}|$ (·····) perturbation components are presented. The DNS solution in baseline conditions (——) is also indicated. The grey-shaded region spanning $0 \leqslant x^* \leqslant 6.4$ represents the range where LPSE and LST results are unavailable.

its amplitude ($|\tilde{u}|$) is maximum, following:

$$\alpha = \alpha_r + i\alpha_i \quad \text{with} \quad \alpha_r = -\frac{\partial\left(\varphi^{A^{\tilde{u}}}\right)}{\partial x}\delta_0 \quad \text{and} \quad \alpha_i = -\frac{\partial\left(\ln A^{\tilde{u}}\right)}{\partial x}\delta_0. \tag{5.1}$$

In (5.1), $\varphi^{A^{\tilde{u}}}$ denotes the phase of the streamwise perturbation component where $|\tilde{u}|$ is maximum, i.e. $\varphi^{A^{\tilde{u}}} = \varphi^{\tilde{u}}(y = \max_y(|\tilde{u}|))$.

Figure 10 shows the growth rate (α_i) and amplitude evolution predicted by the different stability solutions investigated. Upstream of the step, both LPSE and LST accurately capture the perturbation growth rate up to $x^* \approx -20$ (see figure 10*a*). However, as non-parallel effects intensify near the step, the TS growth predicted by LST deviates from the DNS solution earlier than LPSE due to the local formulation of LST. At the step edge ($-20 \leqslant x^* \leqslant 0$ in figure 10*a*), both LST and LPSE fail to capture the strong destabilisation predicted by DNS due to the large base flow streamwise gradients, which invalidate both the LST parallel-flow assumption and the LPSE slowly varying base flow assumption.

Downstream of the step, LPSE and LST are initialised at $x^* = 6.4$. This represents the first streamwise location where the LPSE converges to a physically meaningful

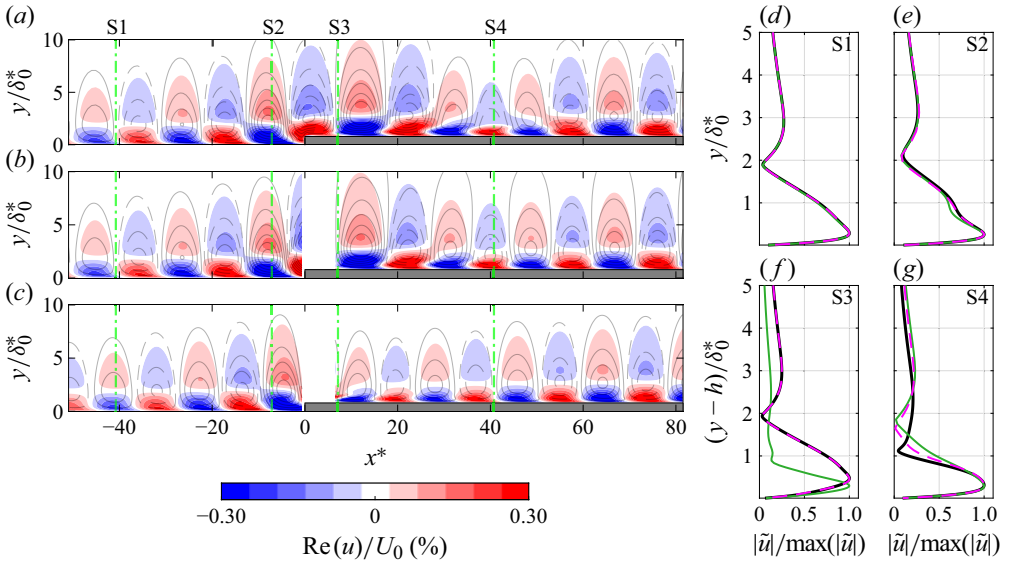

Figure 11. Real part of the streamwise perturbation component (contours) and isolines of the real part of the perturbation streamfunction (contour lines of $\mathrm{Re}(\psi)$, $-5.5\times10^{-6}\leqslant\mathrm{Re}(\psi)/(U_0\delta_0^*)\leqslant5.5\times10^{-6}$) at one TS phase, $\phi=\pi$ rad. Results obtained from (*a*) DNS, (*b*) DNS-initialised LPSE and (*c*) LST. Negative values of $\mathrm{Re}(\psi)$ are indicated with grey solid lines (——), whereas positive values of $\mathrm{Re}(\psi)$ are indicated with grey dashed lines (- - -). Green dash-dotted (-·-·-) vertical lines indicate the streamwise locations where the perturbation profiles in (*d–g*) are extracted. The TS shape function at (*d*) $x^*=-40.8$, (*e*) $x^*=-7.1$, (*f*) $x^*=6.4$ and (*g*) $x^*=40.8$ as obtained from DNS (——), DNS-initialised LPSE (- - -) and LST (——).

solution when the DNS and LST solutions are used as inflow conditions. The inflow perturbation profiles used are shown in figure 11(*f*). Both LST-initialised LPSE and DNS-initialised LPSE results are presented in figure 10. Unlike the aforementioned upstream behaviour, where both LST and LPSE captured similar growth rate trends, DNS-initialised LPSE clearly outperforms LST downstream of the step. Comparison of DNS-initialised LPSE and LST-initialised LPSE with DNS results shows that initialising LPSE with a low-fidelity solution significantly degrades the agreement between DNS and LPSE downstream of the step (compare dashed magenta and dash-dotted blue lines to black lines in figure 10). The DNS-initialised LPSE solution effectively captures the non-monotonic growth-decay-growth pattern downstream. In contrast, both LST and LST-initialised LPSE predict an exponential decay in the growth rate, following the adverse pressure gradient increase downstream (see figure 5*b*), failing to accurately capture the amplitude evolution downstream of the FFS (figure 10*b*). The remarkable agreement between the DNS-initialised LPSE and DNS results highlights the following two key points.

(i) The perturbation behaviour remains linear at the investigated TS wave amplitude.
(ii) Accurately capturing the distortion experienced by the perturbation at the step is essential for describing the downstream evolution of the TS wave.

Figure 11(*a–c*) shows the streamwise perturbation field for the fundamental TS mode as reconstructed from DNS, DNS-initialised LPSE and LST. Additionally, the TS wave shape function obtained from the three different stability solutions is presented in figure 11(*d–g*) for selected streamwise stations (indicated by green vertical lines in figure 11*a–c*).

Results in figure 11(*a–c*) show that the perturbation field from both LPSE and LST present good agreement with the DNS upstream ($x^* \leqslant 0$, see also TS profiles in figure 11*d–e*) and sufficiently downstream of the step ($x^* > 60$). However, in the immediate vicinity downstream of the step ($0 \leqslant x^* \leqslant 60$), while LPSE can capture the tilting of the TS wave structure in the mean shear ($\partial U/\partial y$) direction, LST fails to do so (see figure 11*a–c*). It is important to note that when LPSE is initialised using LST, the resulting perturbation field is similar to LST (not shown here). Thus, the performance of LPSE is largely subject to the shape of the inflow perturbation profile, as already concluded from the growth and amplitude results in figure 10.

The relative fidelity of these methods in capturing the TS wave growth and shape provides further insight into the stability mechanisms dominant in the near region downstream of the step. Specifically, as outlined in the seminal work of Herbert (1997), the LPSE formulation is able to capture pertinent effects of non-parallelism on the evolution of boundary-layer instabilities. In purely parallel mean flows, LPSE results are expected to largely overlap with the local modal solutions of LST. However, when perturbation fields are distorted, the parabolic character of LPSE allows for the upstream history of the flow to travel downstream. This is evident in the close agreement between DNS-initialised LPSE and DNS results, and *vice versa*, in the disagreement between the results of LST and LST-initialised LPSE with DNS, as shown in figure 10. This effectively points to a spatial conditioning of the TS wave at the step towards a new distorted shape that is not an eigensolution of the local flow stability, yet behaves and develops similar to classical TS waves.

5.2. *Non-modal growth*

Results in the previous section reveal that, in order to resolve the perturbation growth downstream of the step using LPSE, it was necessary to initialise the simulation with the DNS perturbation solution. In contrast, initialisation with an eigenvalue solution failed to reproduce the correct perturbation dynamics. This suggests that classical modal eigenvalue approaches are inadequate in the region downstream of the FFS. Therefore, this section investigates potential non-modal growth near the step, following the methodology outlined in Marxen *et al.* (2009).

As evident in figure 10(*a*) in the previous section, the growth of the wall-normal ($\alpha_i^{\tilde{v}}$) and streamwise ($\alpha_i^{\tilde{u}}$) perturbation maxima diverge in the step vicinity. This divergence is evident upstream of the FFS edge ($-20 \leqslant x^* \leqslant 0$) and further downstream, up to $x^* \approx 60$. The decoupling between u- and v-perturbation growth rates is often linked in previous works to the presence of non-modal growth (e.g. Marxen *et al.* 2009; Casacuberta *et al.* 2022, and Michelis *et al.* 2023*b*). Nevertheless, in regions where the base flow streamlines experience significant deflection in wall-normal direction, employing a wall-oriented reference system to distinguish between wall-normal and streamwise perturbation components is no longer deterministic towards identifying regions of non-modal behaviour (Marxen *et al.* 2009). To circumvent this, Marxen *et al.* (2009) decompose the perturbation field using a base flow-oriented coordinate system, as originally proposed by Albensoeder, Kuhlmann & Rath (2001). This approach yields perturbation components that are tangential ($\tilde{v}_t$) and normal ($\tilde{v}_n$) to the local base flow streamlines. The methodology is outlined in the works of Albensoeder *et al.* (2001), Marxen *et al.* (2009), Lanzerstorfer & Kuhlmann (2012) and Casacuberta *et al.* (2022), among others.

Figure 12 illustrates the growth rates of the tangential ($\tilde{v}_t$) and normal ($\tilde{v}_n$) to the base flow perturbation components in baseline and FFS conditions. The corresponding maximum of the two perturbation components is tracked in the streamwise direction to

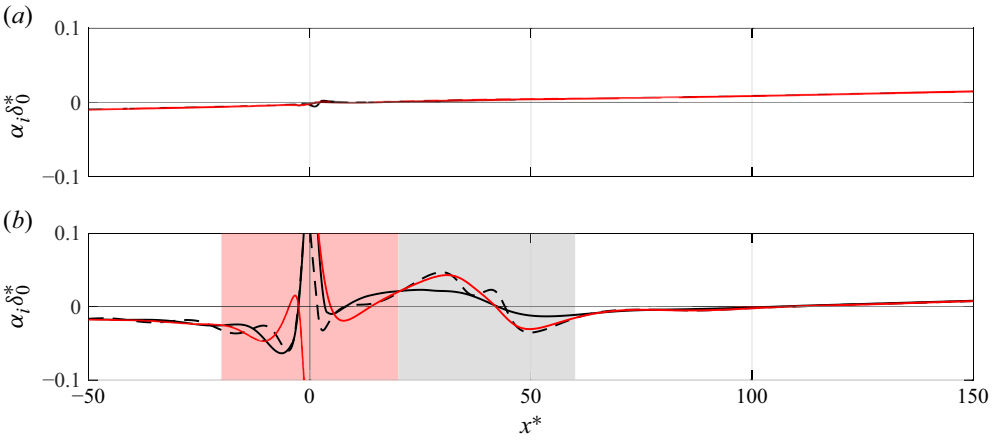

Figure 12. Growth rates of the tangential- ($\alpha_i^{\tilde{v}_t}$, ——) and normal- ($\alpha_i^{\tilde{v}_n}$, ——) to-the-base-flow perturbation maxima in baseline (*a*) and FFS (*b*) conditions. For the tangential perturbation component ($\alpha_i^{\tilde{v}_t}$), solid lines track the TS lower lobe ($\alpha_i^{\tilde{v}_t,\,l}$, ——), whereas dashed lines track the TS upper lobe ($\alpha_i^{\tilde{v}_t,\,u}$, - - -). Red and grey areas indicate the streamwise regions with total (red) and partial (grey) decoupling between $\alpha_i^{\tilde{v}_t}$ and $\alpha_i^{\tilde{v}_n}$. Note that the values of α_i for $-1 \leqslant x^* \leqslant 1$ are excluded from (*b*) for clarity, as significant jumps occur due to the FFS discontinuity.

calculate the corresponding growth rates:

$$\alpha_i^{\tilde{v}_n} = -\frac{1}{A^{\tilde{v}_n}}\frac{\mathrm{d}A^{\tilde{v}_n}}{\mathrm{d}x}, \tag{5.2}$$

$$\alpha_i^{\tilde{v}_t} = -\frac{1}{A^{\tilde{v}_t}}\frac{\mathrm{d}A^{\tilde{v}_t}}{\mathrm{d}x}. \tag{5.3}$$

Owing to the dual peak shape of the streamwise ($\tilde{v}_t$) perturbation component in TS waves, two distinct local maxima are distinguished, namely the lower ($y/\delta_0^* \approx 0.5$) and upper ($y/\delta_0^* \approx 3$) lobe of the TS wave shape function (see, e.g. the different TS maxima in figure 11*d*). This distinction between upper lobe and lower lobe growth rates will be denoted as $\alpha_i^{\tilde{v}_t,\,u}$ and $\alpha_i^{\tilde{v}_t,\,l}$, respectively.

In baseline conditions, both perturbation components exhibit equal growth rates across the entire domain (figure 12*a*), except for a localised region near $x^* \approx 0$, where mild suction is applied in DNS to replicate experimental conditions (see details in § 2.3.1). Conversely, in step conditions, tangential and normal perturbation growth rates present significant deviations.

The decoupling between $\alpha_i^{\tilde{v}_n}$ and $\alpha_i^{\tilde{v}_t}$ observed around $-20 \leqslant x^* \leqslant 60$ from figure 12(*b*) suggests the presence of non-modal growth. In particular, two regions can be identified based on the decoupling behaviour:

(i) In the step vicinity ($-20 \leqslant x^* \leqslant 20$, note red area in figure 12*b*), both upper ($\alpha_i^{\tilde{v}_t,\,u}$) and lower ($\alpha_i^{\tilde{v}_t,\,l}$) lobe growth rates deviate from the normal perturbation growth rate ($\alpha_i^{\tilde{v}_n}$). Hereafter this will be denoted as total decoupling.
(ii) Further downstream ($20 \leqslant x^* \leqslant 60$, note grey area in figure 12*b*), the lower lobe growth rate ($\alpha_i^{\tilde{v}_t,\,l}$) and the normal perturbation growth rate ($\alpha_i^{\tilde{v}_n}$) deviate.

However, the upper lobe growth rate ($\alpha_i^{\tilde{v}_t,\,u}$) converges to $\alpha_i^{\tilde{v}_n}$. Hereafter this behaviour will be denoted as partial decoupling.

In the step vicinity ($-20 \leqslant x^* \leqslant 20$), the total decoupling between $\alpha_i^{\tilde{v}_n}$ and $\alpha_i^{\tilde{v}_t}$ occurs in a region with significant non-parallel effects (e.g. note the abrupt modifications in base flow integral parameters along x^* close to the step in figure 5*c*). Due to the smaller streamwise extent of the FFS-induced base flow distortion compared with the incoming TS wavelength, the latter is scattered (or distorted) by the geometrical discontinuity (Goldstein 1985; Wu & Hogg 2006). The near-wall structure observed after the FFS edge (discussed in § 4.2) reflects the strong distortion experienced by the TS wave. Consistent with these findings, recent studies also report significant non-modal perturbation growth in regions of wave scattering (Michelis *et al.* 2023*a*; Casacuberta *et al.* 2022).

Downstream of the step ($20 \leqslant x^* \leqslant 60$), the partial decoupling observed between $\alpha_i^{\tilde{v}_n}$ and $\alpha_i^{\tilde{v}_t}$ indicates that the TS structure exhibits a stratified growth behaviour in the y direction. The upper part of the TS structure follows a modal evolution, while the lower part is influenced by non-modal growth. This dual behaviour is similar to findings by Marxen *et al.* (2009), where the authors observe non-modal evolution of near-wall streamwise streaks – generated by the lift-up effect – coexisting with a modal (Görtler) instability above. In contrast to Marxen *et al.* (2009), a secondary structure cannot be distinguished herein from the modal TS structure in the lower lobe region (see, e.g. the TS shape in figure 11*g*).

The partial decoupling described in the region $20 \leqslant x^* \leqslant 60$ suggests the presence of non-modal behaviour (Marxen *et al.* 2009). At first glance, this appears to contradict the previously observed agreement (§ 5.1) between DNS and LPSE, given that classical LPSE has been historically associated with the modelling of modal perturbations. However, the LPSE formalism does not solve an eigenvalue problem, but instead propagates a prescribed initial perturbation downstream under the assumption that the dominant streamwise oscillation and growth at each frequency can be represented by a single complex wavenumber (Herbert 1997). As such, LPSE does not necessarily evolve a single mode. It can track a superposition of modes, but only those whose streamwise wavenumbers lie sufficiently close to one another. This interpretation is supported by previous studies in which the LPSE method has also been employed to analyse flows susceptible to non-modal growth, which inherently involve a superposition of modes (Tempelmann, Hanifi & Henningson 2010; Lucas 2014). The observed indications of non-modal behaviour may arise from the streamwise propagation, via the LPSE marching scheme, of a DNS-derived perturbation field composed of a superposition of modes, originating from the strongly non-modal region near the step. The following section investigates further the role of superimposed modes in the DNS solution.

5.3. *Origin of TS wave distortions downstream of the FFS*

This section aims to elucidate the existence and nature of superimposed modes, encoded in the perturbation evolution downstream of the step. To do so, the different eigensolutions from LST applied on the DNS flow in the vicinity of the step are analysed. Figure 13(*a*) shows the real ($\mathrm{Re}(\alpha^n)$) and imaginary ($\mathrm{Im}(\alpha^{\mathrm{n}})$) part of the two least stable eigenvalues predicted by LST for $F = 90$ in the region downstream of the FFS ($x^* \gtrsim 6.4$). The arrows in figure 13(*a*) indicate the direction of variation along the streamwise axis. A second mode (red symbols in figure 13*a*) appears less stable than the classical TS mode (blue circles) closely downstream of the step (see markers of the first streamwise stations in

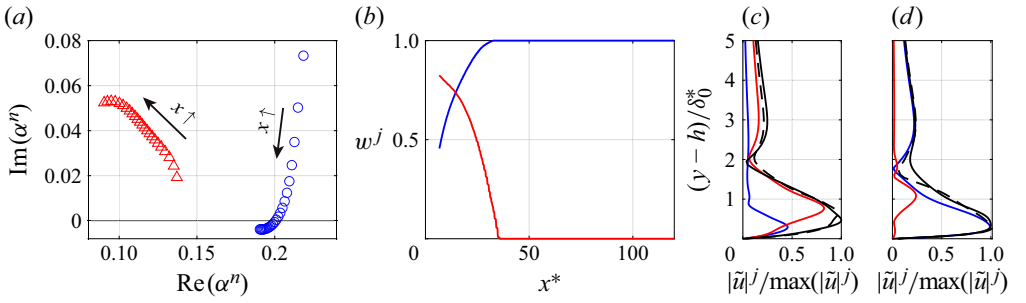

Figure 13. (*a*) Eigenvalues from LST downstream of the step ($6 \leqslant x^* \leqslant 80$). (*b*) Weights assigned to the TS mode (blue, w^1) and second mode (red, w^2) by the non-negative least squares fit. (*c*,*d*) Shape functions of the fundamental mode from DNS (——, $|\tilde{u}|$), weighted TS mode (——, $\hat{\boldsymbol{C}}^1 w^1$), weighted second mode (——, $\hat{\boldsymbol{C}}^2 w^2$) and linear superposition of LST modes (- - -, $\sum_j^2 \hat{\boldsymbol{C}}^j w^j$) at the streamwise locations indicated by black vertical dashed lines in figure 14, namely $x^* = 6.4$ (*c*) and $x^* = 30.5$ (*d*).

figure 13*a*). Nevertheless, it is important to note that this second mode remains stable at all the streamwise stations studied. The TS mode growth rate (α_i) becomes less stable than the second mode's α_i from $x^* > 11.7$ onwards. This second mode, coexisting with the original TS mode, travels in the streamwise direction at a higher phase speed than the original TS wave, owing to its lower $\mathrm{Re}(\alpha)$.

To elucidate whether the superposition of this second mode with the TS mode improves the description of the fundamental mode evolution as predicted by DNS, a methodology inspired by the work of Edelmann (2014) is applied. This involves performing a non-negative least squares fit, where the absolute values of the normalised eigenfunctions of the two modes, shown in figure 13(*c*,*d*), are weighted to minimise the following function:

$$\min_{w^j} \quad \|\hat{\boldsymbol{C}}^j w^j - \hat{\boldsymbol{d}}\|_2^2, \quad \text{subject to} \quad w^j \geqslant 0, \quad j \in \{1, 2\}, \tag{5.4}$$

$$\text{with} \quad \hat{\boldsymbol{C}}^j = \frac{1}{\max(|\tilde{u}_i^j|)} \begin{bmatrix} |\tilde{u}_0|^j \\ |\tilde{u}_1|^j \\ \vdots \\ |\tilde{u}_{n_y}|^j \end{bmatrix}\Bigg|_{\mathrm{LST}} \quad \text{and} \quad \hat{\boldsymbol{d}} = \frac{1}{\max(|\tilde{u}_i|)} \begin{bmatrix} |\tilde{u}_0| \\ |\tilde{u}_1| \\ \vdots \\ |\tilde{u}_{n_y}| \end{bmatrix}\Bigg|_{\mathrm{DNS}}. \tag{5.5}$$

Here the subscript $\|\cdot\|_2$ denotes the Euclidean norm. The term $\hat{\boldsymbol{C}}^j$ represents a column vector containing the normalised eigenfunction of the jth LST mode at a specific x^* station, while w^j is the corresponding weight for the jth mode. Similarly, $\hat{\boldsymbol{d}}$ is a column vector containing the normalised shape function obtained from DNS. Equation (5.4) is minimised independently at each streamwise station x^*, yielding a one-dimensional vector of weights, $\hat{\boldsymbol{w}}^j = [w_0^j, w_1^j, \ldots, w_{n_x}^j]$.

The resulting weights from the optimisation problem are shown in figure 13(*b*). The contribution of the second mode in describing the DNS solution is limited to the region downstream of the step, i.e. $0 \leqslant x^* \leqslant 35$. Similar observations are reported in Edelmann (2014), where the author identified three additional modes that, when superimposed onto the original TS mode, largely contribute to describing the fundamental mode at the region directly downstream of the step. The weighted eigenfunctions, together with the final profile from linear superposition of LST modes ($\hat{\boldsymbol{C}}^1 w^1 + \hat{\boldsymbol{C}}^2 w^2$) are compared with the DNS perturbation profile in figure 13(*c*–*d*) at different x^* stations.

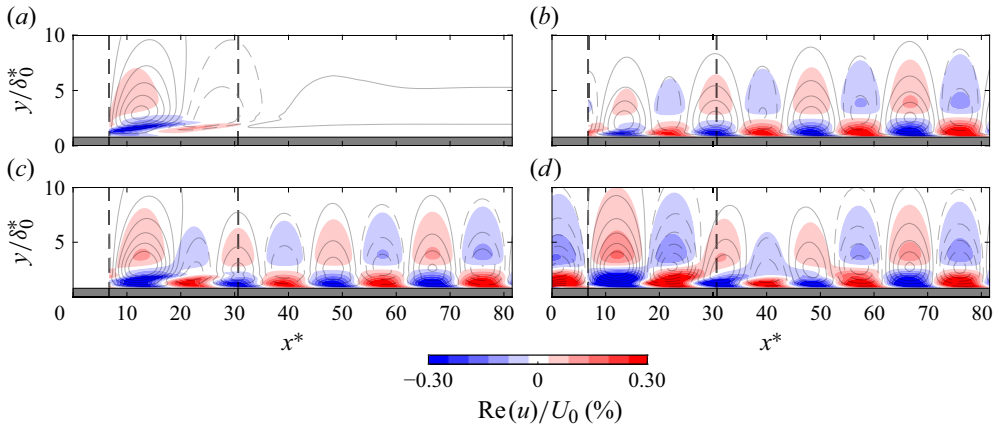

Figure 14. Real part of the streamwise perturbation component (contours) and isolines of the real part of the perturbation streamfunction (contour lines of $\mathrm{Re}(\psi)$, $-5.5\times10^{-6}\leqslant\mathrm{Re}(\psi)/(U_0\delta_0^*)\leqslant5.5\times10^{-6}$) at one TS phase, $\phi=\pi$ rad. Results for the real part of (*a*) the LST second mode, u^2; (*b*) the LST TS mode, u^1; (*c*) the linear superposition of LST modes, u^1+u^2; and (*d*) the DNS solution. Negative values of $\mathrm{Re}(\psi)$ are indicated with grey solid lines (——), whereas positive values of $\mathrm{Re}(\psi)$ are indicated with grey dashed lines (- - -). Black dashed vertical lines indicate streamwise locations for the normalised shape functions shown in figure 13(*c–d*).

The streamwise perturbation field and streamlines for the two LST modes, the reconstructed mode (linear superposition) and the DNS solution are presented in figure 14, where the perturbation velocity for the two LST modes is obtained as

$$q^j = w^j\left(A^{\tilde{q}}_{x_0^*}|_{\mathrm{DNS}}\frac{|\tilde{q}|^j}{\max(|\tilde{q}|^j)}\mathrm{e}^{-\int_{x_0^*}^{x^*}\alpha_i^j dx^*}\mathrm{e}^{i(\varphi^{\tilde{q}^j}+\int_{x_0^*}^{x^*}\alpha_r^j dx^*-\phi)}\right), \tag{5.6}$$

and evaluated at different streamwise stations. In (5.6), $A^{\tilde{q}}_{x_0^*}$ denotes the perturbation amplitude from DNS at the LST inflow, i.e. $x_0^*=6.4$.

In figure 14(*a*) the second mode predicted by LST exhibits a pronounced tilting in the mean shear direction ($\partial U/\partial y$) close to the wall. Interestingly, the topology of this mode resembles the downstream tilted ($\partial y/\partial x|_{\mathrm{Re}(\psi)}>0$ – refer to (5.20) presented later in § 5.4) structures identified in Åkervik *et al.* (2008) as optimal forcing structures initiating TS waves in a 2-D flat-plate boundary layer. Åkervik *et al.* (2008) refer to this structure as the Orr mode, named after the Orr mechanism, which drives the growth of the perturbation field in this context until it converges to the classic modal growth with the emergence of TS waves (see figure 3(c) in Åkervik *et al.* 2008).

The downstream tilting of the second mode helps to describe the topological features observed in DNS immediately downstream of the step (e.g. compare figures 14*c* and 14*d* at $6\leqslant x^*\leqslant30$). However, the reconstructed LST field fails to capture the perturbation evolution in the region of highly parallel flow ($x^*\gtrsim35$), particularly the transition from downstream ($\partial y/\partial x|_{\mathrm{Re}(\psi)}>0$) to upstream ($\partial y/\partial x|_{\mathrm{Re}(\psi)}<0$) tilting around $30\leqslant x^*\leqslant50$. This discrepancy may be attributed to the inherently local nature of LST, which cannot account for the streamwise history of the perturbation. Furthermore, the omission of phase information in the optimisation procedure, as outlined in (5.4), could also contribute to the discrepancy between reconstructed LST and DNS perturbation fields.

Up to this point, the above analysis provides the following insights.

(i) In the region immediately downstream of the step, LST predicts the emergence of a second eigenmode that appears less stable than the original TS mode under the same conditions (figure 13*a*).
(ii) The topological form of the second eigenmode is notably tilted in the mean shear direction (figure 14*a*).
(iii) When reconstructing the DNS perturbation field, the superposition of the spatial structure of the second eigenmode and the original TS wave appear to be encoding the tilted perturbation topology observed in the DNS, which cannot be captured by the original TS mode alone (figures 13*c* and 14*c*).

These findings, together with the outcomes of § 5.1 and § 5.2, indicate that the perturbation distortion observed farther downstream of the FFS ($x^* \gtrsim 10$) is likely a manifestation of the spatial non-modal growth. More specifically, this region can be interpreted as a zone of modes' dominance changeover. Within, the perturbation field is converging towards its modal (asymptotic) state while coexisting with other local eigenmodes generated upstream, near the step ($x^* \lesssim 7$). As the base flow gradually returns to the baseline configuration, these additional modes strongly decay in the streamwise direction (figure 13*a*). However, their influence is encoded in the perturbation field and manifested as the tilting of the perturbation structure. The following section explores how the tilting of the perturbation structure drives the evolution of the perturbation kinetic energy.

5.4. *The role of the Orr mechanism*

The observations presented in the previous sections suggest a region of modes' dominance changeover downstream of the step ($30 \leqslant x^* \leqslant 50$), where the base flow is largely parallel. Notably, in this region the perturbation structure exhibits topological deformations (e.g. figure 9*e*), accompanied by significant changes in growth, in comparison to the baseline case (figure 6*a*). To further clarify whether the perturbation tilting holds connection with the observed inflections in growth (e.g. the region of decay-growth-decay in figure 10*b*), the present section will analyse the evolution of the perturbation kinetic energy around the FFS.

Tollmien–Schlichting waves extract energy from the base flow through a positive Reynolds stress, expressed as

$$\tau = -\langle uv \rangle, \tag{5.7}$$

which is generated by viscosity in the near-wall region (Prandtl 1921). A simplified conceptualisation of the instability mechanics can be found in § 5.2 of Mack (1984), following the original derivation of Prandtl (1921). To better illustrate how the instability exchanges energy with the base flow, it is indicative to examine the production term in the Reynolds–Orr equation (see (1.11) in Schmid & Henningson 2001), which for 2-D flow is given by

$$P = -\int_S u_i u_j \frac{\partial U_i}{\partial x_j} \mathrm{d}S. \tag{5.8}$$

Since this study focuses exclusively on the stability of the fundamental TS mode, the subscript (1,0) has been omitted for simplicity. Substituting the perturbation velocity definition from (4.2) into (5.8) and integrating over one TS wave period, $T = 2\pi/\omega_0$, yields the time-averaged production term:

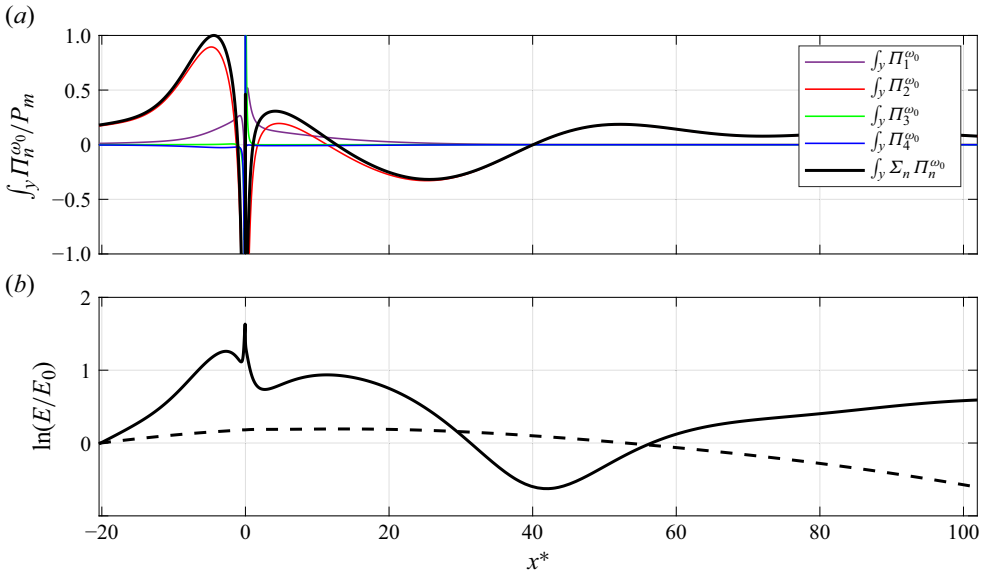

Figure 15. (*a*) Streamwise evolution of the production terms in (5.11)–(5.14) integrated in the y direction. (*b*) Perturbation kinetic energy integrated in the y direction in step (——) and baseline (- - -) conditions. Here P_m denotes the value of $\int_y \sum_n \Pi_n^{\omega_0}$ at $x^* = -5$, the location where $|\int_y \sum_n \Pi_n^{\omega_0}|$ becomes maximum upstream of the step.

$$P_{\omega_0} = -\frac{2\pi}{\omega_0}\int_S (\tilde{u}_i + \text{c.c.})(\tilde{u}_j + \text{c.c.})\frac{\partial U_i}{\partial x_j}\mathrm{d}x\mathrm{d}y. \tag{5.9}$$

Expanding the velocity component multiplication results in

$$P_{\omega_0} = \frac{2\pi}{\omega_0}\int_S \sum_{n=1}^{4} \Pi_n^{\omega_0}\mathrm{d}x\mathrm{d}y, \tag{5.10}$$

where the individual production terms $\Pi_n^{\omega_0}$ are given by

$$\Pi_1^{\omega_0} = -(\tilde{u}\tilde{u}^\dagger + \text{c.c.})\frac{\partial U}{\partial x}, \tag{5.11}$$

$$\Pi_2^{\omega_0} = -(\tilde{u}\tilde{v}^\dagger + \text{c.c.})\frac{\partial U}{\partial y}, \tag{5.12}$$

$$\Pi_3^{\omega_0} = -(\tilde{v}\tilde{u}^\dagger + \text{c.c.})\frac{\partial V}{\partial x}, \tag{5.13}$$

$$\Pi_4^{\omega_0} = -(\tilde{v}\tilde{v}^\dagger + \text{c.c.})\frac{\partial V}{\partial y}. \tag{5.14}$$

Figure 15(*a*) shows the different $\Pi_n^{\omega_0}$ terms in (5.11)–(5.14) integrated in the wall-normal direction. It is apparent from this figure that the term $\Pi_2^{\omega_0}$ (red line in figure 15*a*) constitutes the main contribution to the total production (black line) across the entire domain. This term represents the extraction of energy from the base flow by the disturbance via the build-up of a positive Reynolds stress (τ) averaged over one TS period.

Additionally, comparing figure 15(*a*) with figure 15(*b*) reveals that the evolution of the perturbation kinetic energy can be fully described by examining the production term,

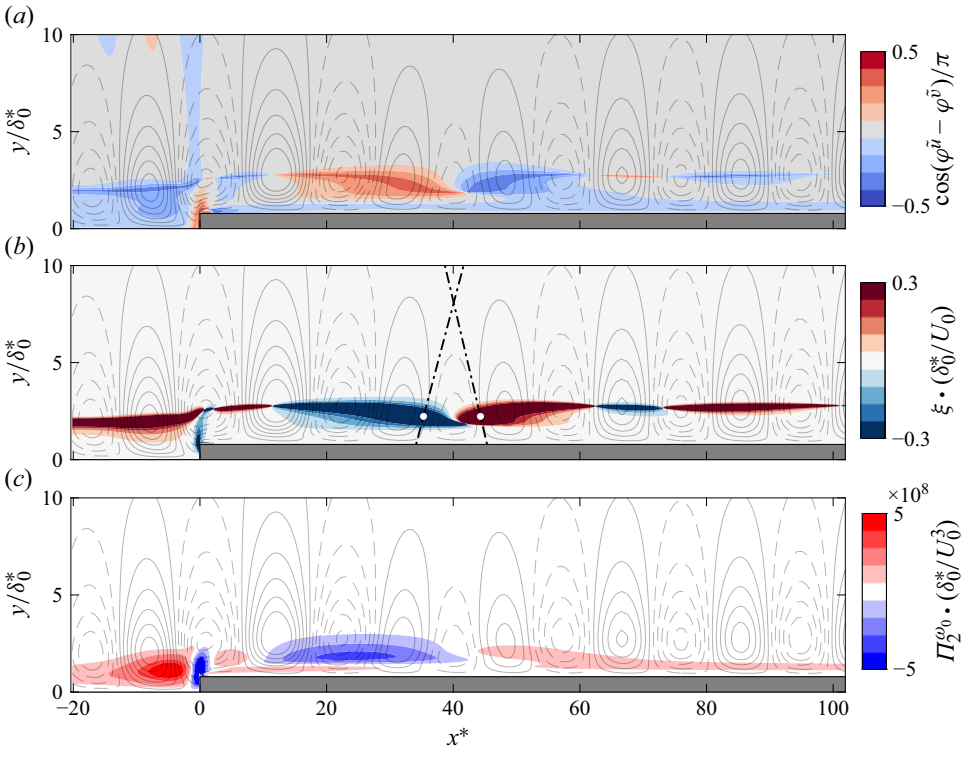

Figure 16. (*a*) Phase difference between streamwise and wall-normal perturbation components, represented by $\cos(\varphi^{\tilde{u}} - \varphi^{\tilde{v}})$. (*b*) Contours of ξ, defined in (5.20). The black dash-dotted lines (-·-·-) indicate the slope of $\mathrm{Re}(\psi)$, represented as $(\partial y/\partial x)_{\mathrm{Re}(\psi)}$. This slope is measured at a fixed wall-normal position ($y/\delta_0^* = 2.2$) but at different streamwise locations ($x^* = 35, 44$), as marked by the white dots. (*c*) Contours of production term, $\Pi_2^{\omega_0}$, as defined in (5.12). Superimposed contour lines represent the real part of the perturbation streamfunction ($-5.5 \times 10^{-6} \leqslant \mathrm{Re}(\psi)/(U_0\delta_0^*) \leqslant 5.5 \times 10^{-6}$) obtained at a specific TS phase, $\phi = 0$. Negative values of $\mathrm{Re}(\psi)$ are indicated with grey solid lines (——), whereas positive values of $\mathrm{Re}(\psi)$ are indicated with grey dashed lines (- - -). All results are in step conditions and obtained from DNS.

i.e. regions of negative production align with regions of perturbation energy decay and *vice versa*. This again reaffirms the linear behaviour of the perturbation field under the conditions concerned herein (i.e. sufficiently low TS wave amplitude).

Equation (5.12) can be alternatively expressed in terms of the perturbation phase and amplitude:

$$\Pi_2^{\omega_0} = -2|\tilde{u}||\tilde{v}| \cos(\varphi^{\tilde{u}} - \varphi^{\tilde{v}}) \frac{\partial U}{\partial y}. \tag{5.15}$$

The previous equation provides insight into the role that the phase shift between $\tilde{u}$ and $\tilde{v}$ plays in regard to the change of sign of the Reynolds stress and thereby in production. The strong distortion observed from the phase contours of $\tilde{u}$ (refer to figure 8*b* in § 4.1) in FFS conditions suggests the emergence of regions downstream of the step where $\tilde{u}$ and $\tilde{v}$ are out of quadrature (i.e. $\varphi^{\tilde{u}} - \varphi^{\tilde{v}} \neq \pm\pi/2$). Consequently, the term $\cos(\varphi^{\tilde{u}} - \varphi^{\tilde{v}})$ in (5.15) approaches values closer to ± 1, leading to either an enhancement or suppression of the Reynolds stresses and, consequently, of the production term $\Pi_2^{\omega_0}$, as shown in figures 16(*a*) and 16(*c*).

To further expose the relationship between the build-up of Reynolds stresses and the topology of the TS wave structure, it is instructive to write the production term $\Pi_2^{\omega_0}$ in terms of the streamfunction, ψ, previously introduced in (4.1). Following the work of Butler & Farrell (1992), it can be shown that by introducing (4.1) into (5.12), $\Pi_2^{\omega_0}$ can be re-expressed as

$$\Pi_2^{\omega_0} = \left(\frac{\partial \tilde{\psi}}{\partial y} \left(\frac{\partial \tilde{\psi}}{\partial x} \right)^{\dagger} + \left(\frac{\partial \tilde{\psi}}{\partial y} \right)^{\dagger} \frac{\partial \tilde{\psi}}{\partial x} \right) \frac{\partial U}{\partial y}, \tag{5.16}$$

$$= 2\mathrm{Re} \left[\left(\frac{\partial \tilde{\psi}}{\partial y} \right)^{\dagger} \frac{\partial \tilde{\psi}}{\partial x} \right] \frac{\partial U}{\partial y}, \tag{5.17}$$

$$= 2\mathrm{Re} \left[\left(\frac{\partial \tilde{\psi}}{\partial y} \right)^{\dagger} \left(\frac{\partial \tilde{\psi}}{\partial y} \right) \left(\frac{\partial \tilde{\psi}/\partial x}{\partial \tilde{\psi}/\partial y} \right) \right] \frac{\partial U}{\partial y}, \tag{5.18}$$

$$= -2\mathrm{Re} \left[|\tilde{u}|^2 \left(\frac{\partial y}{\partial x} \right)_{\tilde{\psi}} \right] \frac{\partial U}{\partial y}. \tag{5.19}$$

Equation (5.19) indicates that, in a boundary layer where the mean flow shear is everywhere positive (i.e. $\partial U/\partial y > 0$, like the case concerned herein), the tilting of the perturbation streamlines ($(\partial y/\partial x)_{\tilde{\psi}}$) uniquely governs the shift of sign of the production term, and therefore, the growth or decay of the instability.

Figure 16(*b*) presents the contours of the product between the mean shear $\partial U/\partial y$ and the slope of the real part of the perturbation streamfunction, $(\partial y/\partial x)_{\mathrm{Re}(\tilde{\psi})}$. This product is denoted as

$$\xi = \frac{\partial U}{\partial y} \left(\frac{\partial y}{\partial x} \right)_{\mathrm{Re}(\tilde{\psi})}. \tag{5.20}$$

According to Butler & Farrell (1992), a perturbation structure tilted in the mean flow shear direction corresponds to $\xi > 0$, whereas a tilt against the mean shear direction is indicated by $\xi < 0$. In this work, upstream and downstream tilting is also employed to refer to regions where $\xi < 0$ and $\xi > 0$, respectively.

To illustrate the relationship between ξ and the topology of the TS wave structure, the real part of the perturbation streamfunction $\mathrm{Re}(\tilde{\psi})$ at a specific TS phase ($\phi = 0$) is also displayed in figure 16(*b*). These results highlight how changes in the sign of ξ correlate with variations in the tilting of the TS structures, represented by isolines of $\mathrm{Re}(\tilde{\psi})$. Similarly, the contours of the production component $\Pi_2^{\omega_0}$ are shown in figure 16(*c*) superimposed with $\mathrm{Re}(\tilde{\psi})$. In this case, this visualisation helps to establish a link between the tilting of the TS structures and the shift in the sign of production, indicating either growth or decay.

Upstream of the step, ξ becomes negative, indicating a tilting of the perturbation streamlines against the mean shear direction as a result of the strong base flow distortion exerted by the adverse pressure gradient. This upstream tilting ($\xi < 0$) creates a positive production ($\Pi_2^{\omega_0} > 0$, (5.19)) that enhances the growth of the instability, as observed from figure 15(*a*). Upon reaching the step corner, the perturbation streamlines are strongly bent when they encounter the step edge. The distortion imposed by the step on the perturbation

induces a locally negative production ($\Pi_2^{\omega_0} < 0$) that yields a stabilising effect; see the contours of $\Pi_2^{\omega_0}$ in figure 16(*c*).

While the increase and decrease of production (i.e. build-up of positive and negative Reynolds stresses, respectively) in the step neighbourhood can be attributed to the strong distortion experienced by the perturbation streamlines due to the abrupt base flow modification, observations downstream of the step do not obey the same reasoning since the base flow is largely parallel there. Comparison between contours of ξ in figure 16(*b*) and contours of $\Pi_2^{\omega_0}$ in figure 16(*c*) in the region between $20 \leqslant x^* \leqslant 60$ reveal a good correlation between the shift from negative to positive production values and the shift from downstream ($\xi > 0$) to upstream ($\xi < 0$) tilting. Based on previous works (Orr 1907; Butler & Farrell 1992), the growth of disturbances as a result of their tilting against the shear can be associated to the Orr mechanism. This mechanism is known to be most effective for disturbances featuring finite streamwise wavenumbers, like TS waves (Hwang, Moin & Hack 2021).

The Orr mechanism consists of the amplification of both streamwise and wall-normal perturbation components due to an increase in the perturbation's circulation as it changes orientation relative to the mean shear (Hwang *et al.* 2021). However in contrast to exponential growth, the Orr mechanism amplifies both normal and tangential perturbation components in an algebraic manner, i.e. in a non-modal fashion (Orr 1907; Butler & Farrell 1992). This is in line with the decoupling observed between the growth rates of tangential- ($\alpha_i^{\tilde{v}_t}$) and normal- ($\alpha_i^{\tilde{v}_n}$) to-the-base-flow perturbation components in figure 12(*b*). Finally, a comment can be made on the role of the Orr mechanism in the specific conditions of FFS flows. Traditionally, the Orr mechanism is usually associated with the destabilisation of the perturbation field. An example of this is the work of Åkervik *et al.* (2008), where the evolution of a wavepacket tilted against the mean shear leads to the linear amplification of the perturbation via the Orr mechanism, eventually developing into a TS wave. However, the present results unveil an unconventional role for the Orr mechanism, as it is observed to be responsible also for the local decay of the perturbation.

6. Conclusions

The impact of a FFS on the stability of TS waves, together with the mechanisms governing modifications in the perturbation field, has been investigated through experiments and 2-D DNS. Detailed HWA and PIV measurements of the time-averaged flow and the perturbation field around the step facilitate a comprehensive comparison between experiments and DNS. The observed excellent agreement between experiments and 2-D DNS validates the 2-D nature of the interaction and supports the use of 2-D DNS for in-depth diagnostics at the step to understand the mechanisms in play in the TS–FFS interaction. Further comparison between 2-D DNS, LST and LPSE is conducted to elucidate the stability characteristics and mechanisms active at the step. The excellent agreement between DNS and LPSE results, both upstream and downstream of the step in regions where the base flow remains parallel, confirms the linear behaviour of the perturbation field under the TS wave amplitudes studied.

Upstream of the FFS, TS waves undergo exponential amplification due to the adverse pressure gradient build-up upstream of the FFS. Both tangential- ($\alpha_i^{\tilde{v}_t}$) and normal- ($\alpha_i^{\tilde{v}_n}$) to-the-base-flow perturbation components exhibit equivalent growth rates, indicating that the destabilisation follows a modal behaviour (Marxen *et al.* 2012). Both LPSE and LST capture the perturbation growth upstream of $x^* = -20$, beyond where the base flow starts to exhibit significant non-parallel effects. The observed TS destabilisation behaviour

remains similar to that seen upstream of laminar separation bubbles (Dovgal *et al.* 1994) or smooth roughness elements, such as humps (Park & Park 2013).

In the FFS vicinity, both DNS and experiments capture a strong non-parallel behaviour of the mean flow due to abrupt jumps in the pressure gradient (i.e. adverse-favourable-adverse). The streamwise extent over which the mean flow is distorted is significantly smaller than the incoming TS wavelength, leading to scattering (or distortion) of the instability (Xu *et al.* 2017). This distortion is evident in PIV and HWA measurements, as well as in DNS, manifesting as significant modifications in the perturbation amplitude and phase fields compared with baseline conditions. Furthermore, analysis of the base flow-oriented perturbation component growth reveals a strong decoupling between $\alpha_i^{\tilde{v}_n}$ and $\alpha_i^{\tilde{v}_t}$, indicating non-modal perturbation evolution (Marxen *et al.* 2009; Casacuberta *et al.* 2022). In this region, neither LPSE nor LST can resolve the rapid perturbation evolution due to their intrinsic assumptions. Nevertheless, evaluating LST immediately downstream of the step reveals a second mode that appears less stable (i.e. $\alpha_i^2 < \alpha_i^1$) than the TS mode close to the step. In combination, these results suggest that the distortion of the perturbation field close to the step obeys a non-modal behaviour.

At the step edge, DNS results reveal the emergence of a near-wall structure locked at opposite phase and opposite streamfunction ($\mathrm{Re}(\psi)$) sign with respect to the incoming TS wave. The amplitude of this structure decays in the x direction and merges closely downstream with the TS structure above. The presence of this secondary structure does not appear to affect the growth of the pre-existent TS wave. Similar to the mechanisms presented by Casacuberta *et al.* (2025), which explain the onset of near-wall streaks at the FFS edge with S-CFI, the origin of the near-wall structure observed here is attributed to the redistribution of streamwise perturbation momentum by the wall-normal perturbation component in a region of high mean flow shear.

Downstream of the step, the mean flow resumes its parallel behaviour; however, the perturbation field remains significantly distorted, evident from the tilting of the TS structures both in and against the mean flow shear direction. In this region, the decoupling between the growth of normal ($\alpha_i^{\tilde{v}_n}$) and tangential ($\alpha_i^{\tilde{v}_t}$) perturbation components is confined to the lower lobe of the TS wave, indicating a dual growth behaviour (modal and non-modal) stratified in the y direction. Interestingly, LPSE accurately captures the growth evolution downstream of the step, but only when initialised with the DNS distorted perturbation profile shortly after the FFS edge. Linear stability theory results in this region indicate that the relevance of any superimposed mode decays in the x direction due to the recovery of the base flow to parallel conditions. Taken together, these results suggest that the perturbation field is undergoing a region of slowly varying spatial transient growth, i.e. a region of modes changeover. The impact (or history) of any superimposed modes arising at the highly non-parallel step region is propagated downstream and captured by LPSE, imprinting modifications (in the form of perturbation tilting) in the perturbation field even far downstream of the step.

The tilting of the perturbation structure downstream of the step is accompanied by changes in growth, specifically the perturbation undergoes growth-decay-growth. In this region, the perturbation evolution is governed by the Orr mechanism. In particular, where the perturbation structure tilts in the mean flow shear direction ($\xi > 0$), the perturbation decays, and conversely, it amplifies when it tilts against the mean shear ($\xi < 0$), eventually realigning to an asymptotic (modal) TS structure. Similar to Teng's (2023) findings, this study also identifies a strong stabilising region downstream of the step, in a region where the perturbation structure appears tilted in the mean shear direction ($\xi > 0$). However, in

contrast to Teng's (2023) work, no stabilisation below baseline conditions or transition delay is observed in the DNS results or experiments, respectively.

The outcomes of the present work demonstrate that the presence of superimposed modes influences locally the perturbation growth and structure in the vicinity of the step, particularly downstream. However, under the specific FFS conditions examined, the perturbation field eventually collapses back to the classical TS wave shape far downstream of the step. This suggests that the eventual laminar breakdown process (not resolved in the present work) will remain consistent with the classical TS transition pathway (i.e. path A in Morkovin, Reshotko & Herbert 1994).

Future studies should focus on investigating the underlying physical mechanisms downstream of the step, especially at higher FFS heights as well as higher initial TS amplitudes, where both nonlinear and non-modal effects are expected to become more pronounced. Such studies could reveal TS–FFS interaction scenarios where the transition pathway deviates from the classical TS route. Furthermore, such investigations could contribute to identify additional functional parameters that improve the universality of ΔN-based transition prediction models.

Supplementary movie. Supplementary movie is available at https://doi.org/10.1017/jfm.2025.10768.

Acknowledgements. The authors sincerely thank S. Bernardy, E. Langedijk, and P. Duyndham for their technical support and guidance. Special recognition is given to J. Casacuberta for his valuable insights into the role of non-modal growth in the presence of a FFS. Additionally, the authors deeply appreciate the stimulating scientific discussions with Dr. M. Kloker, S. Westerbeek, Y. Chen and A. Synodinos, which significantly enriched this work.

Funding. The first author, M. Barahona, acknowledges the financial support of the Department of Flow Physics and Technology at TU Delft. The authors M. Barahona, Dr. A.F. Rius-Vidales, and Prof. Dr. M. Kotsonis acknowledge the support of the European Research Council (grant number 803082). Finally, the authors F. Tocci and Dr. S. Hein gratefully acknowledge the scientific support and HPC resources provided by the German Aerospace Center (DLR). The HPC system CARO is partially funded by the Ministry of Science and Culture of Lower Saxony and the Federal Ministry for Economic Affairs and Climate Action. Open access funding provided by Delft University of Technology.

Declaration of interests. The authors report no conflict of interest.

References

Åkervik, E., Ehrenstein, U., Gallaire, F. & Henningson, D.S. 2008 Global two-dimensional stability measures of the flat plate boundary-layer flow. *Eur. J. Mechan.-B/Fluids* **27** (5), 501–513.

Albensoeder, S., Kuhlmann, H.C. & Rath, H.J. 2001 Three-dimensional centrifugal-flow instabilities in the lid-driven-cavity problem. *Phys. Fluids* **13** (1), 121–135.

Batchelor, G.K. 2000 *An Introduction to Fluid Dynamics*. Cambridge University Press.

Butler, K.M. & Farrell, B.F. 1992 Three-dimensional optimal perturbations in viscous shear flow. *Phys. Fluids A: Fluid Dyn.* **4** (8), 1637–1650.

Casacuberta, J., Hickel, S., Westerbeek, S. & Kotsonis, M. 2022 Direct numerical simulation of interaction between a stationary crossflow instability and forward-facing steps. *J. Fluid Mech.* **943**, A46.

Casacuberta, J., Westerbeek, S., Franco, J.A., Groot, K.J., Hickel, S., Hein, S. & Kotsonis, M. 2025 Streaky perturbations in swept-wing flow over forward-facing step. *Phys. Rev. Fluids* **10** (2), 023902.

Chauvat, G. 2020 Receptivity, stability and sensitivity analysis of two-and three-dimensional flows. PhD thesis, KTH Royal Institute of Technology.

Costantini, M. 2016 Experimental analysis of geometric, pressure gradient and surface temperature effects on boundary-layer transition in compressible high Reynolds number flows. PhD thesis, Rheinisch-Westfälische Technische Hochschule Aachen.

Costantini, M., Risius, S. & Klein, C. 2022 Step-induced transition in compressible high Reynolds number flow. *Flow* **2**, E33.

CROUCH, J.D., KOSORYGIN, V.S. & NG, L.L. 2006 Modeling the effects of steps on boundary-layer transition. In *IUTAM Symposium on Laminar-Turbulent Transition*, pp. 37–44. Springer.

CROUCH, J.D., KOSORYGIN, V.S., SUTANTO, M.I. & MILLER, G.D. 2022 Characterizing surface-gap effects on boundary-layer transition dominated by Tollmien–Schlichting instability. *Flow* **2**, E8.

DONG, M. & ZHANG, A. 2018 Scattering of Tollmien–Schlichting waves as they pass over forward-/backward-facing steps. *Appl. Math. Mechan.* **39** (10), 1411–1424.

DOVGAL, A.V., KOZLOV, V.V. & MICHALKE, A. 1994 Laminar boundary layer separation: instability and associated phenomena. *Prog. Aerosp. Sci.* **30** (1), 61–94.

DOWNS, R.S. & FRANSSON, J.H.M. 2014 Tollmien–Schlichting wave growth over spanwise-periodic surface patterns. *J. Fluid Mech.* **754**, 39–74.

DRAKE, A., BENDER, A., KORNTHEUER, A., WESTPHAL, R., ROHE, W., DALE, G., MCKEON, B. & GERASCHCHENKO, S. 2010 Step excrescence effects for manufacturing tolerances on laminar flow wings. In *48th AIAA Aerospace Sciences Meeting Including the New Horizons Forum and Aerospace Exposition*. AIAA 2010-375.

DRAKE, A., BENDER, A. & WESTPHAL, R. 2008 Transition due to surface steps in the presence of favorable pressure gradients. In *26th AIAA Applied Aerodynamics Conference*. AIAA 2008-7334.

EDELMANN, C.A. 2014 Influence of forward-facing steps on laminar-turbulent transition. PhD thesis, University of Stuttgart.

EPPINK, J.L. 2020 Mechanisms of stationary cross-flow instability growth and breakdown induced by forward-facing steps. *J. Fluid Mech.* **897**, A15.

FISCHER, P.F., LOTTES, J.W. & KERKEMEIER, S.G. 2008 Nek5000 web page, Available at http://nek5000.mcs.anl.gov.

FRANCO, J.A., HEIN, S. & VALERO, E. 2020 On the influence of two-dimensional hump roughness on laminar–turbulent transition. *Phys. Fluids* **32** (3), 034102.

GOLDSTEIN, M.E. 1985 Scattering of acoustic waves into Tollmien–Schlichting waves by small streamwise variations in surface geometry. *J. Fluid Mech.* **154**, 509–529.

HANSEN, H. 2010 Laminar flow technology—the Airbus view. In *27th International Congress of the Aeronautical Sciences (ICAS)*.

HERBERT, T. 1997 Parabolized stability equations. *Annu. Rev. Fluid Mech.* **29** (1), 245–283.

HOLMES, B.J., OBARA, C.J., MARTIN, G.L. & DOMACK, C.S. 1985 Manufacturing tolerances for natural laminar flow airframe surfaces. *SAE Trans.* 522–531.

HULTMARK, M. & SMITS, A.J. 2010 Temperature corrections for constant temperature and constant current hot-wire anemometers. *Meas. Sci. Technol.* **21** (10), 105404.

HWANG, H., MOIN, P. & HACK, M.J.P. 2021 A mechanism for the amplification of interface distortions on liquid jets. *J. Fluid Mech.* **911**, A51.

JOSLIN, R.D. 1998 Aircraft laminar flow control. *Annu. Rev. Fluid Mech.* **30** (1), 1–29.

LANZERSTORFER, D. & KUHLMANN, H.C. 2012 Three-dimensional instability of the flow over a forward-facing step. *J. Fluid Mech.* **695**, 390–404.

LIN, N., REED, H.L. & SARIC, W.S. 1992 Effect of leading-edge geometry on boundary-layer receptivity to freestream sound. In *Instability, Transition, and Turbulence*, pp. 421–440. Springer.

LUCAS, J.M. 2014 Spatial optimal perturbations for transient growth analysis in three-dimensional boundary layers. PhD thesis, Université de Toulouse.

MACK, L.M. 1984 Boundary-layer linear stability theory. *Tech. Rep.* AGARD-R-709. Advisory Group for Aerospace Research and Development (AGARD), Neuilly-sur-Seine, France, part of: special course on stability and transition of laminar flow,

MARXEN, O., LANG, M. & RIST, U. 2012 Discrete linear local eigenmodes in a separating laminar boundary layer. *J. Fluid Mech.* **711**, 1–26.

MARXEN, O., LANG, M., RIST, U., LEVIN, O. & HENNINGSON, D.S. 2009 Mechanisms for spatial steady three-dimensional disturbance growth in a non-parallel and separating boundary layer. *J. Fluid Mech.* **634**, 165–189.

MERINO-MARTÍNEZ, R., CARPIO, A.R., PEREIRA, L.T.L., VAN HERK, S., AVALLONE, F., RAGNI, D. & KOTSONIS, M. 2020 Aeroacoustic design and characterization of the 3D-printed, open-jet, anechoic wind tunnel of Delft University of Technology. *Appl. Acoust.* **170**, 107504.

METHEL, J., FORTE, M., VERMEERSCH, O. & CASALIS, G. 2022 Experimental investigation on the effect of forward-facing steps and gaps combined with wall suction on boundary layer transition. *Exp. Fluids* **63**, 1–17.

MICHELIS, T., DE KONING, C. & KOTSONIS, M. 2023*a* On the interaction of Tollmien–Schlichting waves with a wall-embedded Helmholtz resonator. *Phys. Fluids* **35** (3).

MICHELIS, T., PUTRANTO, A.B. & KOTSONIS, M. 2023*b* Attenuation of Tollmien–Schlichting waves using resonating surface-embedded phononic crystals. *Phys. Fluids* **35** (4).
MORKOVIN, M.V., RESHOTKO, E. & HERBERT, T. 1994 Transition in open flow systems – a reassessment. *Bull. Am. Phys. Soc.* **39**, 1882.
NENNI, J.P. & GLUYAS, G.L. 1966 Aerodynamic design and analysis of an LFC surface. *Astronaut. Aeronaut.* **4** (7), 52.
ORR, W.M. 1907 The stability or instability of the steady motions of a perfect liquid and of a viscous liquid. Part II: A viscous liquid. *Proc. Royal Irish Acad. A* **27**, 69–138.
PARK, D. & PARK, S.O. 2013 Linear and non-linear stability analysis of incompressible boundary layer over a two-dimensional hump. *Comput. Fluids* **73**, 80–96.
PERRAUD, J., ARNAL, D. & KUEHN, W. 2014 Laminar-turbulent transition prediction in the presence of surface imperfections. *Intern. J. Engine. Syst. Model. Simulat.* **6** (3-4), 162–170.
PERRAUD, J. & SERAUDIE, A. 2000 Effects of steps and gaps on 2D and 3D transition. In *European Congress on Computational Methods in Applied Science and Engineering*, pp. 11–14, ECCOMAS.
PLACIDI, M., GASTER, M. & ATKIN, C.J. 2020 Acoustic excitation of Tollmien–Schlichting waves due to localised surface roughness. *J. Fluid Mech.* **895**, R5.
PRANDTL, L. 1921 Bemerkungen über Die Entstehung der Turbulenz. *ZAMM-J. Appl. Math. Mechan./Zeitschrift für Angewandte Mathematik und Mechanik* **1** (6), 431–436.
RIUS-VIDALES, A.F. & KOTSONIS, M. 2020 Influence of a forward-facing step surface irregularity on swept wing transition. *AIAA J.* **58** (12), 5243–5253.
RIUS-VIDALES, A.F. & KOTSONIS, M. 2021 Impact of a forward-facing step on the development of crossflow instability. *J. Fluid Mech.* **924**, A34.
RIZZETTA, D.P. & VISBAL, M.R. 2014 Numerical simulation of excrescence generated transition. *AIAA J.* **52** (2), 385–397.
ROUVIERE, A. 2023 Amélioration des modèles de tolérance de surface pour les couches limites en s'appuyant sur des outils d'intelligence artificielle. PhD thesis, ISAE-SUPAERO.
SARIC, W.S., WEI, W. & RASMUSSEN, B.K. 1995 Effect of leading edge on sound receptivity. In *Laminar-Turbulent Transition*, pp. 413–420. Springer.
SARIC, W.S., WEI, W. & RASMUSSEN, B.K. 2007 Boundary-layer stability and transition. In *Handbook of Experimental Fluid Mechanics* (ed. C. Tropea, A. L. Yarin & J. F. Foss), pp. 886–896. Springer.
SCHMID, P.J. & HENNINGSON, D.S. 2001 *Stability and Transition in Shear Flows*. Springer.
SCHRAUF, G. 2005 Status and perspectives of laminar flow. *Aeronaut. J.* **109**, 639–644.
SCHRAUF, G. 2018 On allowable step heights: Lessons learned from the F100 and ATTAS flight tests. In *Proceedings of the 6th European Conference on Computational Mechanics (ECCM 6) and 7th European Conference on Computational Fluid Dynamics (ECFD 7)*, ECCM-ECFD.
SCHULTZ, M.P. & FLACK, K.A. 2007 The rough-wall turbulent boundary layer from the hydraulically smooth to the fully rough regime. *J. Fluid Mech.* **580**, 381–405.
SCIACCHITANO, A., SCARANO, F. & WIENEKE, B. 2012 Multi-frame pyramid correlation for time-resolved PIV. *Exp. Fluids* **53**, 1087–1105.
SOMMERFELD, A. 1909 *Ein Beitrag zur Hydrodynamischen Erklaerung der Turbulenten Fluessigkeitsbewegungen*. vol. 3. Accademia dei Lincei, pp. 116–124.
STRATFORD, B.S. 1959 An experimental flow with zero skin friction throughout its region of pressure rise. *J. Fluid Mech.* **5** (1), 17–35.
TEMPELMANN, D., HANIFI, A. & HENNINGSON, D.S. 2010 Spatial optimal growth in three-dimensional boundary layers. *J. Fluid Mech.* **646**, 5–37.
TENG, M. 2023 Effects of surface imperfections on the transitional boundary layer. *Phys. Fluids* **35** (8).
TOCCI, F., FRANCO, J.A., HEIN, S., CHAUVAT, G. & HANIFI, A. 2021 The effect of 2D surface irregularities on laminar-turbulent transition: A comparison of numerical methodologies. In *New Results in Numerical and Experimental Fluid Mechanics XIII: Contributions to the 22nd STAB/DGLR Symposium*, pp. 246–256. Springer.
TUFTS, M.W., REED, H.L., CRAWFORD, B.K., DUNCAN, G.T.Jr & SARIC, W.S. 2017 Computational investigation of step excrescence sensitivity in a swept-wing boundary layer. *J. Aircraft* **54** (2), 602–626.
WANG, Y.X. & GASTER, M. 2005 Effect of surface steps on boundary layer transition. *Exp. Fluids* **39** (4), 679–686.
WESTERBEEK, S. 2020 Development of a nonlinear parabolized stability equation (NPSE) analysis tool for spanwise invariant boundary layers. Master thesis, Delft University of Technology.
WHITE, E.B., SARIC, W.S. & RADEZTSKY, R.H. 2000 Leading-edge acoustic receptivity measurements using a pulsed-sound technique. In *Laminar-Turbulent Transition*, pp. 103–108. Springer.

WÖRNER, A., RIST, U. & WAGNER, S. 2003 Humps/steps influence on stability characteristics of two-dimensional laminar boundary layer. *AIAA J.* **41** (2), 192–197.

WU, X. & DONG, M. 2016 A local scattering theory for the effects of isolated roughness on boundary-layer instability and transition: transmission coefficient as an eigenvalue. *J. Fluid Mech.* **794**, 68–108.

WU, X. & HOGG, L.W. 2006 Acoustic radiation of Tollmien–Schlichting waves as they undergo rapid distortion. *J. Fluid Mech.* **550**, 307–347.

XU, H., LOMBARD, J.E.W. & SHERWIN, S.J. 2017 Influence of localised smooth steps on the instability of a boundary layer. *J. Fluid Mech.* **817**, 138–170.